Medical Image Analysis 59 (2020) 101566

Contents lists available at ScienceDirect

Medical Image Analysis

journal homepage: www.elsevier.com/locate/media

Model-Based High-Definition Dynamic Contrast Enhanced MRI for Concurrent Estimation of Perfusion and Microvascular Permeability

Joon Sik Park[a], Eunji Lim[a], Seung-Hong Choi[d], Chul-Ho Sohn[d], Joonyeol Lee[a,c], Jaeseok Park[a,b,*]

[a] Department of Biomedical Engineering, Sungkyunkwan University, 2066, Seobu-Ro, Jangan-Gu, Suwon, Republic of Korea
[b] Biomedical Institute for Convergence, Sungkyunkwan University, Suwon, Republic of Korea
[c] Center for Neuroscience Imaging Research, Institute for Basic Science, Suwon, Republic of Korea
[d] Department of Radiology, Seoul National University Hospital, Seoul, Republic of Korea

ARTICLE INFO

Article history:
Received 22 March 2019
Revised 20 September 2019
Accepted 26 September 2019
Available online 8 October 2019

Keywords:
Magnetic resonance imaging
Dynamic contrast enhanced
High definition
Microvascular permeability
Brain cancer

ABSTRACT

This work introduces a model-based, high-definition dynamic contrast enhanced (DCE) MRI for concurrent estimation of perfusion and microvascular permeability over the whole brain. A time series of reference-subtracted signals is decomposed into one component that reflects main contrast dynamics and the other one that includes residual contrast agents (CA) and background signals. The former is described by linear superposition of a finite number of basic vectors trained from an augmented set of data that consists of tracer-kinetic model driven signal vectors and patient-specific measured ones. Contrast dynamics is estimated by solving a constrained optimization problem that incorporates the linearized signal decomposition into the measurement model of DCE MRI and then combining the main component with the background-suppressed, residual CA signals. To the best of our knowledge, this is the first work that prospectively enables rapid temporal sampling with 1.5 s (3∼4 times higher than clinical routines) while simultaneously achieving high isotropic spatial resolution with 1.0 mm^3 (4∼6 times higher than routines), enhancing estimation of both patient-specific inputs and outputs for quantification of microvascular functions. Simulations and experiments are performed to demonstrate the effectiveness of the proposed method in patients with brain cancer.

1. Introduction

Dynamic contrast enhanced (DCE) magnetic resonance imaging (MRI) (Sourbron et al., 2009; Dutoit et al., 2013) has been widely used in a clinical routine to investigate vascular structures and functions (perfusion, microvascular permeability) for pathological tissues in the presence of leakages from capillaries. Particularly in the brain, it has become an essential tool to assess blood-brain-barrier (BBB) leakages in tumors (Roberts et al., 2000), multiple sclerosis lesions (Ingrisch et al., 2012), stroke (Merali et al., 2017), and dementia (Van De Haar et al., 2016). In DCE MRI, a time series of three-dimensional (3D) T_1-weighted images is typically acquired to describe contrast dynamics (wash-in, a rise to a maximum peak, wash-out) after intravenously administering T_1-shortening contrast agents (CA). The contrast dynamics in each voxel is reflected in time-varying MR signal intensities, which are then converted to concentration time courses of CA by utilizing linear relation between concentration of CA and change of T_1 relaxation rate. A tracer-kinetic model (Sourbron and Buckley, 2011; 2013), which employs a concentration time course in an arterial region as an input, is fitted to those in tissues of interest (output), revealing some of the following hidden parameters related to tissue perfusion and microvascular permeability: plasma flow (F_p), plasma volume fraction (v_p), permeability-surface area product (PS), and interstitial volume fraction (v_e). The F_p is the flow of plasma into the capillary bed, and the v_p is the volume fraction inside the capillary bed. PS indicates the flow of molecules through the capillary membranes in a certain volume of tissue and the v_e is the fraction of interstitial volume that contained in a volume of tissue. In general, F_p and v_p are regarded as perfusion parameters, while PS and v_e are known as permeability parameters. In general, F_p and v_p are regarded as perfusion parameters, while PS and v_e are known as permeability parameters. Accurate estimation of the perfusion parameters requires high temporal resolution to capture rapidly varying signal intensities during the first pass of bolus when CA remains mostly in the blood stream. On the other hand, to precisely estimate the permeability parameters, data acquisition is to be length-

* Corresponding author.
E-mail address: jaeseokpark.biel@gmail.com (J. Park).

https://doi.org/10.1016/j.media.2019.101566
1361-8415/

ened to accommodate a slow uptake of CA into interstitial spaces. Thus, to improve estimation of both perfusion and microvascular permeability, DCE MRI requires a sufficiently long acquisition time with high temporal resolution.

Simplified tracer-kinetic models such as the extended Tofts model (Tofts and Kermode, 1991) and the Patlak model (Hackstein et al., 2005) have been widely used for various clinical applications, in which the former enables estimation of v_p, the volume transfer constant K^{trans} (a mixture of F_p and PS), and v_e by assuming $F_p = \infty$ (neglecting plasma transit time) while the latter is a special case of the former and produces v_p and K^{trans} with the following constraints: $F_p = \infty$ and no backflux from interstitial spaces. Despite the partial success of describing an uptake of CA, a capillary transit time is neglected, which may not reflect underlying tissue physiology in a real setting. Furthermore, the strong constraints preclude concurrent estimation of F_p and PS, leading to mixed information of perfusion and permeability. To address this issue, complex models with four unknown parameters (F_p, v_p, PS', v_e), which include the two-compartment exchange model (2CXM) (Brix et al., 2004), the tissue homogeneity model (TH)(Simpson et al., 1999), the adiabatic approximation to the tissue homogeneity model (AATH) (St.Lawrence and Ting-Yim, 1998), and the distributed parameter model (DP) (Garpebring et al., 2009), can be employed but require a highly defined uptake curve of CA with high temporal resolution during data acquisition (O'Connor et al., 2007). It was shown in (Kershaw and Cheng, 2010) that a temporal resolution of at least 1.5 s is needed to reliably estimate all perfusion and permeability parameters with minimal bias.

In all tracer-kinetic models of DCE MRI, two distinct time-resolved signals need to be measured in an arterial region (input) and tissues of interest (output), respectively. The arterial input function (AIF), which estimates the concentration of CA in an artery feeding the corresponding tissue of interest, exhibits rapid contrast dynamics with time, while the output function changes slowly due to a gradual uptake of CA in capillary plasma and interstitial spaces. Thus, it is very important to precisely capture the two distinct contrast dynamics: rapidly varying AIF and slowly varying output signals. Given the above signal characteristics, dual resolution approaches in DCE MRI (Jelescu et al., 2011; Li et al., 2012) were recently introduced, in which the AIF was measured using high temporal resolution and low spatial resolution while the output function was sampled using low temporal resolution and high spatial resolution. However, the measured AIF, which is sampled with low spatial resolution, potentially suffers from partial volume effects (van Osch et al., 2005), corrupting the measurement of the rapidly-rising upslope during the first pass of bolus and thereby resulting in erroneous parameter estimates. Additionally, contrast dynamics in tissues is typically quite slow, but is known to be substantially fast in tumors due to high vasculature and rapid transfer between capillaries and interstitial spaces (Choyke et al., 2003; Jansen et al., 2008). Thus, to estimate the two distinct contrast dynamics in arterial regions and tissues of interest, high-definition DCE MRI with high spatial and temporal resolution is needed. To address this issue, DCE MRI was combined with parallel imaging and compressed sensing for brain (Lebel et al., 2014; Otazo et al., 2015; Guo et al., 2016; 2017), liver (Feng et al., 2014), and prostate (Rosenkrantz et al., 2015) using high undersampling in $k-t$ space and nonlinear reconstruction with sparsity priors. Among them, only a few studies (Lebel et al., 2014; Guo et al., 2016; 2017) demonstrated the feasibility of the whole-brain DCE MRI for tumor characterization with prospectively enhanced spatial and temporal resolution: $0.94 \times 0.94 \times 1.9\,\text{mm}^3$, 4.1 s in (Lebel et al., 2014; Guo et al., 2016); $0.9 \times 0.9 \times 1.9\,\text{mm}^3$, 5.0 s in (Guo et al., 2017). Nevertheless, as suggested in (Kershaw and Cheng, 2010), temporal resolution needs to be further increased.

Given the above considerations, in this work we develop a model-based, high-definition DCE MRI to enable concurrent estimation of perfusion and microvascular permeability over the whole brain. A time-series of reference-subtracted signals is decomposed into: one component that reflects main contrast dynamics and the other one that includes residual CA and background signals. The former is described by linear superposition of a finite number of basic vectors trained from an augmented set of data that consists of tracer-kinetic model driven signal vectors and patient-specific measured ones. Contrast dynamics is estimated by solving a constrained optimization problem that incorporates the linearized signal decomposition model into the highly undersampled measurement model of DCE MRI with sparsity priors while combining the resulting main component with the residual background-suppressed CA signals. To the best of our knowledge, this is the first work that prospectively enables rapid temporal sampling with 1.5 s ($3 \sim 4$ times higher than clinical routines) while simultaneously achieving high isotropic spatial resolution with $1.0\,\text{mm}^3$, ($4 \sim 6$ times higher than clinical routines), enhancing estimation of both patient-specific inputs and outputs for quantification of microvascular functions. Simulations and in vivo experiments are performed to validate the effectiveness of the proposed method in brain cancer.

The rest of the paper is organized as follows: In Section 2, we introduce the notations used throughout the paper, and present a measurement model in DCE MRI, a linearized signal decomposition model specific to DCE MRI, and a detailed algorithm on estimating contrast dynamics from incomplete measurements for quantification of microvascular function parameters. In Section 3, simulations and experimental studies are described. Lastly, in Section 4, discussion and conclusion are presented.

2. Method

2.1. Notations

Notations, which are used throughout the paper, are listed in Table 1. Matrices, vectors, and scalars are denoted by boldface uppercase letters, boldface lowercase letters, and italics, respectively. $\mathbb{C}$ and $\mathbb{R}$ denote a set of complex and real values, respectively.

2.2. Measurement Model in DCE MRI

After intravenously injecting CA into the blood stream, a series of time-resolved, CA-induced signal modulation, which represents contrast dynamics of interest, is captured voxel-by-voxel. The corresponding measurement model in DCE MRI is described by:

$$y_l(\mathbf{k}, t) = \int c_l(\mathbf{r}) x(\mathbf{r}, t) e^{-j\mathbf{k}\cdot\mathbf{r}} d\mathbf{r} + n_l(\mathbf{k}, t) \tag{1}$$

where $y_l(\mathbf{k}, t)$ is the measured DCE signal at the Fourier encoding index $\mathbf{k}$ and the time t for the lth receiver coil; $c_l(\mathbf{r})$ is the spatially varying coil sensitivity at the spatial position $\mathbf{r}$ for the lth coil that is assumed to remain invariant with time; $x(\mathbf{r}, t)$ is the target signal in the spatial and temporal domain, representing a desired, time-varying DCE signal in each voxel; $n_l(\mathbf{k}, t)$ is the measurement noise for the lth coil with complex white Gaussian distribution.

A DCE MR image at a specific temporal phase (t) in Eq. (1) is column-vectorized by $\mathbf{x}_t = \left[x(\mathbf{r}_0, t)\; x(\mathbf{r}_1, t) \ldots x(\mathbf{r}_{N_t-1}, t)\right]^T$. The entire DCE MR image in the $x-t$ space, $\mathbf{X} = \left[\mathbf{x}_0\; \mathbf{x}_1\; \ldots \mathbf{x}_{N_t-1}\right]$, can be

Table 1
Notations and their Descriptions

Notations	Descriptions
k, x, t	k-space, spatial, and temporal domains, respectivelyt
N, N_t, N_c, M	Lengths of spatial, temporal, coil, and measured Fourier encoding dimensions, respectively
$\mathbf{Y} \in \mathbb{C}^{MN_c \times N_t}$	Measured signal matrix in k-t space
$\mathbf{X} \in \mathbb{C}^{NN_c \times N_t}$	Target signal matrix in x-t space
$\mathbf{X_0} \in \mathbb{C}^{NN_c \times 1}$	Baseline signal matrix in x-t space
$\mathbf{X_D} \in \mathbb{C}^{NN_c \times N_t}$	Main DCE signal matrix in x-t space
$\mathbf{X_B} \in \mathbb{C}^{NN_c \times N_t}$	Residual DCE signal matrix in x-t space
$\overline{\mathbf{X}}_\mathbf{B} \in \mathbb{C}^{NN_c \times N_t}$	Background suppressed, residual signal matrix in x-t space
$\mathbf{U} \in \mathbb{C}^{T \times r}$	Spatial basis of $\mathbf{X_D}$ with a rank of r
$\mathbf{V}_r \in \mathbb{C}^{N_t \times r}$	Temporal basis of $\mathbf{X_D}$ with a rank of r
$\mathbf{X_P} \in \mathbb{R}^{N \times N_p}$	Residual pre-contrast background signal matrix
$\mathbf{X_E} \in \mathbb{R}^{N \times N_e}$	Residual augmented background signal matrix
$\mathbf{U_B} \in \mathbb{R}^{(N_p+N_e) \times r}$	Spatial basis of residual background signal matrix
$\mathcal{F}_u : \mathbb{C}^{NN_c \times N_t} \rightarrow \mathbb{C}^{MN_c \times N_t}$	Undersampled Fourier encoding operator
$\mathcal{S} : \mathbb{C}^{N \times N_t} \rightarrow \mathbb{C}^{NN_c \times N_t}$	Coil sensitivity operator.
$\mathbb{E} : \mathbb{C}^{N \times N_t} \rightarrow \mathbb{C}^{MN_c \times N_t}$	Sensitivity encoding operator.

written in a Casorati matrix form by:

$$\mathbf{X} = \begin{bmatrix} x(\mathbf{r}_0, t_0) & \dots & x(\mathbf{r}_0, t_{N_t-1}) \\ \vdots & \ddots & \vdots \\ x(\mathbf{r}_N, t_0) & \dots & x(\mathbf{r}_N, t_{N_t-1}) \end{bmatrix} \tag{2}$$

where N is the total number of voxels in each temporal phase, and N_t is the total number of temporal phases.

Given the Casorati form of the spatiotemporal signal representation in $x-t$ space, measured signals in a specific temporal phase (t) are correspondingly column-vectorized by $\mathbf{y}_{l,t} = [y_l(\mathbf{k}_0, t)\, y_l(\mathbf{k}_1, t)) \dots y_l(\mathbf{k}_{M-1}, t)]^T$ where M is the total number of Fourier encodings in each temporal phase; $\mathbf{y}_{l,t}$ is subsequently stacked in the temporal dimension column-wise, resulting in $\mathbf{Y}_l = \left[\mathbf{y}_{l,0}\, \mathbf{y}_{l,1} \dots \mathbf{y}_{l,N_t-1}\right]$; $\mathbf{Y}_l$ is then put in the coil dimension row-wise, yielding $\mathbf{Y} = \left[\mathbf{Y}_0\, \mathbf{Y}_1 \dots \mathbf{Y}_{N_c-1}\right]^T$ where N_c is the total number of receiver coils. With the measured matrix $\mathbf{Y}$ ($\in \mathbb{C}^{MN_c \times N_t}$) and the desired target matrix $\mathbf{X}$ ($\in \mathbb{C}^{NN_c \times N_t}$), the measurement model of DCE MRI in Eq. (1) is then recast in a matrix form by:

$$\begin{aligned} \mathbf{Y} &= \mathcal{F}_u \mathcal{S}(\mathbf{X}) + \mathbf{N} \\ &= \mathbb{E}(\mathbf{X}) + \mathbf{N} \end{aligned} \tag{3}$$

where $\mathcal{F}_u : \mathbb{C}^{NN_c \times N_t} \rightarrow \mathbb{C}^{MN_c \times N_t}$ is the spatial Fourier encoding operator with incomplete sampling ($M \ll N$) in $k-t$ space; $\mathcal{S} : \mathbb{C}^{N \times N_t} \rightarrow \mathbb{C}^{NN_c \times N_t}$ is the coil sensitivity mapping operator that performs column-vectorization of coil sensitivity profiles in each coil by $\mathbf{c}_l = [c(\mathbf{r}_0)\, c(\mathbf{r}_1) \dots c(\mathbf{r}_{N-1})]^T$, applies the Hadamard product between $\mathbf{c}_l$ and $\mathbf{x}_t$ and stacks in the temporal dimension column-wise by $\mathbf{S}_l = \left[\mathbf{c}_l \odot \mathbf{x}_0\, \mathbf{c}_l \odot \mathbf{x}_1 \dots \mathbf{c}_l \odot \mathbf{x}_{N_t-1}\right]$, and then puts $\mathbf{S}_l$ in the coil dimension row-wise by $\mathbf{S} = \left[\mathbf{S}_0\, \mathbf{S}_1 \dots \mathbf{S}_{N_c-1}\right]^T$; $\mathbf{N}$ is the noise matrix; $\mathbb{E} : \mathbb{C}^{N \times N_t} \rightarrow \mathbb{C}^{MN_c \times N_t}$ is the sensitivity encoding operator that is equal to $\mathcal{F}_u \mathcal{S}$.

A spoiled gradient echo (GRE) MR pulse sequence, which encodes steady state signals by repeating radio-frequency pulses with a uniform interval, is typically used in acquiring a time series of DCE data while intravenously injecting CA (O'Connor et al., 2011). Hence, due to the steady state signal acquisition, temporal signal modulation in DCE MRI results only from time-varying concentration of CA that subsequently produces changes in T_1 relaxation times for tissues of interest. Thus, the measurement model in Eq. (1) can then be recast by employing a steady state signal and its corresponding temporal modulation as:

$$\begin{aligned} y_l(\mathbf{k}, t) &= \int c_l(\mathbf{r}) \hat{x}(\mathbf{r}) \mathcal{G}(T_1(\mathbf{r}, t)) e^{-j\mathbf{k}\cdot\mathbf{r}} d\mathbf{r} + n_l(\mathbf{k}, t) \\ \mathcal{G}(T_1(\mathbf{r}, t)) &= \frac{\sin\alpha \left(1 - e^{-\mathrm{TR}/T_1(\mathbf{r},t)}\right)}{1 - \cos\alpha\, e^{-\mathrm{TR}/T_1(\mathbf{r},t)}} \end{aligned} \tag{4}$$

where $\hat{x}(\mathbf{r})$ is the steady state signal in each voxel; $\mathcal{G}(T_1(\mathbf{r}, t))$ is the nonlinear temporal signal modulation resulting from time-varying T_1 relaxation times; α is the flip angle of RF pulse; TR is the time interval between neighboring RF pulses. However, it may be difficult to find an optimal solution by minimizing data consistency errors due to the nonlinearity with respect to $T_1(t)$ and the potential scale mismatch between $\hat{x}(\mathbf{r})$ and $T_1(\mathbf{r}, t)$ as shown in (Block et al., 2007).

2.3. Linearized Signal Decomposition Model

Prior to injection of CA in DCE MRI, a set of pre-contrast reference can be constructed by employing either full sampling in a single phase or interleaved sampling followed by averaging over multiple time phases. With varying concentration of CA, a time series of the reference-subtracted signal vectors is arranged column-wise in a Casorati matrix form, which can then be separated into one matrix that reflects contrast dynamics in $x-t$ space and the other matrix that contains residual background signals. Given the above considerations, the proposed signal model in DCE MRI is decomposed by:

$$\mathbf{R_X} = \mathbf{X} - \mathbf{X_0} = \mathbf{X_D} + \mathbf{X_B} + \mathbf{N} \tag{5}$$

where $\mathbf{R_X}$ is the reference-subtracted signal matrix; $\mathbf{X}_0$ is the reference signal matrix that consists of time-invariant baseline vectors; $\mathbf{X_D}$ is the main matrix that contains CA induced signal variations with time voxel by voxel; $\mathbf{X_B}$ is the additive matrix that denotes residual background signals other than CA induced signals.

While CA in the blood stream flows into capillary plasma space, permeates into interstitial space, and then exchanges between the two spaces, signal intensities typically vary smoothly in a correlated fashion with time. This implies that the row vectors in the matrix $\mathbf{X_D}$ can be described by linearly combining a finite set of the right singular vectors of the matrix $\mathbf{X_D}$ corresponding to large singular values in terms of singular value decomposition (SVD). To find the temporal basis, a set of training data is constructed, in which tracer-kinetic model driven signals are row-vectorized and then stacked row-wise with changing the following parameters: F_p, v_p, PS, and v_e. In this work, one of the four-parameter models, 2CXM (Khalifa et al., 2014), in DCE MRI is chosen as a tracer-kinetic model to include concurrent effects of perfusion and microvascular permeability on temporal signal evolutions. Signals in the central region of $k-t$ space, which contain main contrast dynamics, are typically acquired with full sampling. Measured signals in the corresponding central $k-t$ space from each patient with brain cancer are augmented to the tracer-kinetic model driven training data row-wise to reflect actual temporal signal patterns. Lastly,

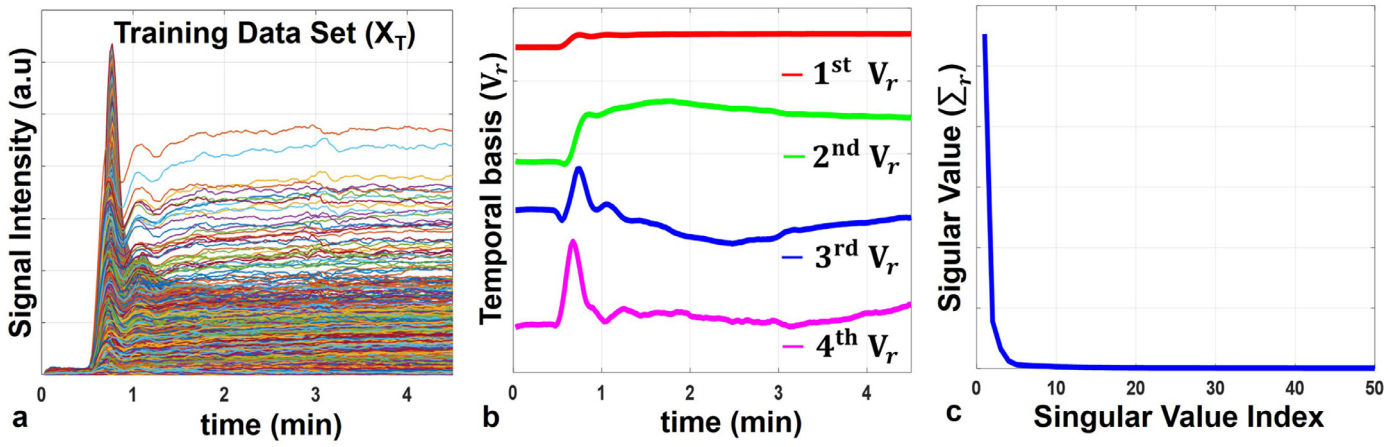

Fig. 1. A time series of the augmented training data in $\mathbf{X_T}$ (a), a set of the corresponding basic vectors of the temporal basis in $\mathbf{V_r}$ (b), and the corresponding singular values in $\mathbf{\Sigma}_r$ (c). Note that singular values in (c) decrease rapidly with increasing index.

the tracer-kinetic model driven signal vectors are temporally readjusted to reflect an actual bolus delay specific to each patient using an intersectional time point of the most rapidly varying, measured signal vector. The temporal basis is then calculated by performing SVD on the training data matrix and taking a portion of the corresponding right singular vectors by:

$$\mathbf{X_T} = \begin{bmatrix} \mathbf{X_{sim}} \\ \mathbf{X_{meas}} \end{bmatrix} \xrightarrow{\text{SVD}} \mathbf{U}_r \Sigma_r \mathbf{V}_r^H \tag{6}$$

where $\mathbf{X_T}$ ($\in \mathbb{R}^{T\times N_t}$) is the training data matrix consisting of the tracer-kinetic model driven signal matrix ($\mathbf{X_{sim}}$) and the measured signal matrix in the central portion of $k-t$ space ($\mathbf{X_{meas}}$); T is the total number of row vectors in the training data; $\mathbf{U}_r$ ($\in \mathbb{R}^{T\times r}$) is the unitary matrix that contains the left singular vectors corresponding to the r largest singular values; $\mathbf{\Sigma}_r$ ($\in \mathbb{R}^{r\times r}$) is the diagonal matrix that contains the r corresponding singular values; $\mathbf{V}_r$ ($\in \mathbb{R}^{N_t\times r}$) is the unitary matrix that contains the corresponding right singular vectors, representing the desired temporal basis. $\mathbf{X_T}$, $\mathbf{V}_r$, and Σ_r are graphically illustrated in Fig. 1a–c.

Given the linear basis, $\mathbf{V}_r$, as a priori, the proposed signal model in Eq. (5) can be rewritten by decomposing $\mathbf{X_D}$ into the two matrices that contain spatial and temporal information, respectively, as:

$$\begin{aligned} \mathbf{R_X} &= \mathbf{X_D} + \mathbf{X_B} + \mathbf{N} \\ \mathbf{X_D} &= \mathbf{U}\mathbf{V}_r^H \end{aligned} \tag{7}$$

where $\mathbf{U}$ contains the spatial information of $\mathbf{X_D}$, which is complementary to $\mathbf{V}_r$, the temporal information of $\mathbf{X_D}$. In the presence of the two distinct contrast dynamics, rapidly varying input signals in an arterial region and slowly varying output signals in tissues, the proposed low rank model, $\mathbf{U}\mathbf{V}_r^H$, in Eq. (5) may not capture details on the former signal pattern, depending on the rank r. As a result, the additive matrix $\mathbf{X_B}$ contains residual contrast dynamics that is missing in $\mathbf{X_D}$ as well as non-contrast background artifacts. Thus, the proposed signal decomposition model in Eq. (7) is advantageous in that it provides a framework to recapture residual contrast dynamics without apparent loss of information during reconstruction in the next section particularly in case the low rank model in $\mathbf{X_D}$ may broaden a profile of the AIF.

2.4. Reconstruction of Contrast Dynamics from Incomplete Measurements

In this section, we introduce a reconstruction framework of contrast dynamics that incorporates the proposed, linearized signal decomposition model in Eq. (7) into the measurement model in Eq. (3) while being formulated as a constrained minimization problem with multiple sparsity priors using the following objective function:

$$\begin{aligned} \mathcal{J}(\mathbf{U}, \mathbf{X_D}, \mathbf{X_B}) &= ||\mathcal{F}_t(\mathbf{X_D})||_1 + \lambda_U ||\psi(\mathbf{U})||_1 + \lambda_B ||\mathcal{F}_t(\mathbf{X_B})||_1 \\ \text{s.t.} \quad \mathbf{R_Y} &= \mathbf{Y} - \mathbf{Y}_0 = \mathbb{E}(\mathbf{X_D} + \mathbf{X_B}) \\ \mathbf{X_D} &= \mathbf{U}\mathbf{V}_r^H \end{aligned} \tag{8}$$

where $\mathcal{F}_t : \mathbb{C}^{N\times N_t} \to \mathbb{C}^{N\times N_t}$ is the temporal Fourier transform operator; $\mathcal{F}_t(\cdot)$ denotes the sparse representation of the argument in $x-f$ space; $\psi : \mathbb{C}^{N\times r} \to \mathbb{C}^{N\times r}$ is the discrete wavelet transform operator; λ_U and λ_B are the balancing parameters that control sparsities among $\mathcal{F}_t(\mathbf{X_D})$, $\psi(\mathbf{U})$, and $\mathcal{F}_t(\mathbf{X_B})$; $\mathbf{R_Y}$ ($\in \mathbb{C}^{MN_c\times N_t}$) is the residual signal matrix in $k-t$ space that is constructed by subtracting the baseline (pre-contrast) measured signal matrix ($\mathbf{Y}_0$) from the measured DCE signal matrix ($\mathbf{Y}$). Coil sensitivity maps included in the sensitivity encoding operator ($\mathbb{E}$) are estimated using the fully acquired baseline data, in which each coil k-space is low-pass filtered and inverse Fourier transformed, and each resulting coil image is then normalized by root-sum-of-squared combination of all coil images.

The objective function in Eq. (8) is reformulated into an unconstrained optimization problem using the associated augmented Lagrange multiplier (ALM) function (Boyd et al., 2011) with additional balancing parameters by:

$$\begin{aligned} \mathcal{L}(\mathbf{U}, \mathbf{X_D}, \mathbf{X_B}, \mathbf{\Gamma_1}, \mathbf{\Gamma_2}) &= \mathcal{J}(\mathbf{U}, \mathbf{X_D}, \mathbf{X_B}) \\ &+ \frac{\lambda_1}{2} \left\| \mathbf{R_Y} - \mathbb{E}(\mathbf{X_D} + \mathbf{X_B}) + \frac{1}{\lambda_1}\mathbf{\Gamma_1} \right\|_F^2 \\ &+ \frac{\lambda_2}{2} \left\| \mathbf{X_D} - \mathbf{U}\mathbf{V}_r^H + \frac{1}{\lambda_2}\mathbf{\Gamma_2} \right\|_F^2 \end{aligned} \tag{9}$$

where $\mathbf{\Gamma_1}$, and $\mathbf{\Gamma_2}$ are the Lagrange variables, and λ_1 and λ_2 are the additional balancing parameters. Since multiple unknown variables are included in Eq. (9), in this work a framework of the alternating direction method of multiplier (ADMM) (Wang et al., 2008; Goldstein and Osher, 2009; Lingala et al., 2011) is chosen to minimize the corresponding ALM function with respect to $\mathbf{U}$, $\mathbf{X_D}$, and $\mathbf{X_B}$, in which $\mathbf{U}$, $\mathbf{X_D}$, and $\mathbf{X_B}$ are estimated in an alternating fashion while retaining the other variables obtained in the previous step, and the Lagrange multipliers (Γ_1 and Γ_2) are then updated at each iteration. Given the above considerations, the ADMM yields the following separable subproblems and corresponding solutions for $\mathbf{U}$, $\mathbf{X_D}$, and $\mathbf{X_B}$ at the $(k+1)^{\text{th}}$ iteration step:

$$\begin{aligned}\mathbf{U}^{(k+1)} &= \arg\min_{\mathbf{U}} \mathcal{L}(\mathbf{U}, \mathbf{X}_\mathbf{D}^{(k)}, \mathbf{X}_\mathbf{B}^{(k)}, \mathbf{\Gamma}_1^{(k)}, \mathbf{\Gamma}_2^{(k)}) \\ &= \arg\min_{\mathbf{U}} \lambda_U \|\psi(\mathbf{U})\|_1 + \frac{\lambda_2}{2}\left\|\mathbf{X}_\mathbf{D}^{(k)} - \mathbf{U}\mathbf{V}_r^H + \frac{1}{\lambda_2}\mathbf{\Gamma}_2^{(k)}\right\|_F^2 \\ &= \psi^*\left(\mathcal{S}_{\lambda_U \delta_\mathbf{U}}\left[\psi\left\{\mathbf{U}^{(k)} + \delta_\mathbf{U}\lambda_2\left(\mathbf{X}_\mathbf{D}^{(k)} - \mathbf{U}^{(k)}\mathbf{V}_r^H + \frac{1}{\lambda_2}\mathbf{\Gamma}_2^{(k)}\right)\mathbf{V}_r\right\}\right]\right) \end{aligned} \tag{10}$$

$$\begin{aligned}\mathbf{X}_\mathbf{D}^{(k+1)} &= \arg\min_{\mathbf{X}_\mathbf{D}} \mathcal{L}(\mathbf{U}^{(k+1)}, \mathbf{X}_\mathbf{D}, \mathbf{X}_\mathbf{B}^{(k)}, \mathbf{\Gamma}_1^{(k)}, \mathbf{\Gamma}_2^{(k)}) \\ &= \arg\min_{\mathbf{X}_\mathbf{D}} \|\mathcal{F}_t(\mathbf{X}_\mathbf{D})\|_1 + \frac{\lambda_1}{2}\left\|\mathbf{R}_\mathbf{Y} - \mathbb{E}(\mathbf{X}_\mathbf{D} + \mathbf{X}_\mathbf{B}^{(k)}) + \frac{1}{\lambda_1}\mathbf{\Gamma}_1^{(k)}\right\|_F^2 \\ &\quad + \frac{\lambda_2}{2}\left\|\mathbf{X}_\mathbf{D} - \mathbf{U}^{(k+1)}\mathbf{V}_r^H + \frac{1}{\lambda_2}\mathbf{\Gamma}_2^{(k)}\right\|_F^2 \\ &= \mathcal{F}_t^*\left(\mathcal{S}_{\delta_{\mathbf{X}_\mathbf{D}}}\left[\mathcal{F}_t\left\{\mathbf{X}_\mathbf{D}^{(k)} + \delta_{\mathbf{X}_\mathbf{D}}\lambda_1\mathbb{E}^*\left(\mathbf{R}_\mathbf{Y} - \mathbb{E}(\mathbf{X}_\mathbf{D}^{(k)} + \mathbf{X}_\mathbf{B}^{(k)}) + \frac{1}{\lambda_1}\mathbf{\Gamma}_1^{(k)}\right)\right.\right.\right. \\ &\quad \left.\left.\left. + \delta_{\mathbf{X}_\mathbf{D}}\lambda_2\left(\mathbf{X}_\mathbf{D}^{(k)} - \mathbf{U}^{(k+1)}\mathbf{V}_r^H + \frac{1}{\lambda_2}\mathbf{\Gamma}_2^{(k)}\right)\right\}\right]\right) \end{aligned} \tag{11}$$

$$\begin{aligned}\mathbf{X}_\mathbf{B}^{(k+1)} &= \arg\min_{\mathbf{X}_\mathbf{M}} \mathcal{L}(\mathbf{U}^{(k+1)}, \mathbf{X}_\mathbf{D}^{(k+1)}, \mathbf{X}_\mathbf{B}, \mathbf{\Gamma}_1^{(k)}, \mathbf{\Gamma}_2^{(k)}) \\ &= \min_{\mathbf{X}_\mathbf{M}} \lambda_B\|\mathcal{F}_t(\mathbf{X}_\mathbf{B})\|_1 + \frac{\lambda_1}{2}\left\|\mathbf{R}_\mathbf{Y} - \mathbb{E}(\mathbf{X}_\mathbf{D}^{(k+1)} + \mathbf{X}_\mathbf{B}) + \frac{1}{\lambda_1}\mathbf{\Gamma}_1^{(k)}\right\|_F^2 \\ &= \mathcal{F}_t^*\left(\mathcal{S}_{\lambda_B\delta_{\mathbf{X}_\mathbf{M}}}\left[\mathcal{F}_t\left\{\mathbf{X}_\mathbf{B}^{(k)} + \delta_{\mathbf{X}_\mathbf{B}}\lambda_1\mathbb{E}^*\left(\mathbf{R}_\mathbf{Y} - \mathbf{E}(\mathbf{X}_\mathbf{D}^{(k+1)} + \mathbf{X}_\mathbf{B}^{(k)})\right.\right.\right.\right. \\ &\quad \left.\left.\left.\left. + \frac{1}{\lambda_1}\mathbf{\Gamma}_1^{(k)}\right)\right\}\right]\right) \end{aligned} \tag{12}$$

$$\mathbf{\Gamma}_1^{(k+1)} = \mathbf{\Gamma}_1^{(k)} + \lambda_1\left(\mathbf{R}_\mathbf{Y} - \mathbb{E}(\mathbf{X}_\mathbf{D}^{(k+1)} + \mathbf{X}_\mathbf{B}^{(k+1)})\right) \tag{13}$$

$$\mathbf{\Gamma}_2^{(k+1)} = \mathbf{\Gamma}_2^{(k)} + \lambda_2\left(\mathbf{X}_\mathbf{D}^{(k+1)} - \mathbf{U}^{(k+1)}\mathbf{V}_r^H\right) \tag{14}$$

where $\delta_\mathbf{U}$, $\delta_{\mathbf{X}_\mathbf{D}}$, and $\delta_{\mathbf{X}_\mathbf{B}}$ are the step sizes with iterations; $\mathcal{F}_t^*$ is the adjoint operator of $\mathcal{F}_t$; ψ^* is the adjoint operator of ψ; $\mathcal{S}_\tau$ is the soft thresholding operator that is equivalent to the proximal operator of ℓ_1 norm by:

$$\mathcal{S}_\tau(z) = \begin{cases} z(|z| - \tau)/|z| & \text{if } |z| \geq \tau \\ 0 & \text{otherwise} \end{cases} \tag{15}$$

where τ is the thresholding value for $\mathcal{S}_\tau$. Given $\mathbf{U}^{(k+1)}$, $\mathbf{X}_\mathbf{D}^{(k+1)}$ and $\mathbf{X}_\mathbf{B}^{(k+1)}$, the Lagrange variables are updated as shown in Eqs. (13) and (14). Iterations in the above ADMM method continue with the following stopping criterion: $\left\|\mathbf{X}_\mathbf{D}{}^{(k+1)} - \mathbf{X}_\mathbf{D}{}^{(k)}\right\|_F^2 \leq \delta\left\|\mathbf{X}_\mathbf{D}{}^{(k)}\right\|_F^2$ or $k > K_{\max}$ where δ and $K_{\max}$ are the predefined error tolerance and the maximum number of iterations, respectively. The proposed model-based reconstruction of contrast dynamics from incomplete measurement is summarized in Algorithm 1.

2.5. Capturing Residual Contrast Dynamics with Background Suppression

The low rank model in Eq. (7) may not be able to describe detailed information on rapid contrast dynamics particularly in arterial regions. In the proposed reconstruction framework, both residual contrast dynamics and background signals are then captured in the additive matrix $\mathbf{X}_\mathbf{B}$. To restore residual contrast dynamics while further suppressing background signals, in this section a finite set of basic vectors, which can represent only background signals other than residual CA induced signals, is found under the assumption that background signals mainly result from motion-mismatch induced signal differences between time frames.

Algorithm 1. Model-based reconstruction of contrast dynamics from incomplete measurements in DCE MRI.

1. Task: Find $\mathbf{X}_\mathbf{D}$, $\overline{\mathbf{X}}_\mathbf{B}$, and $\mathbf{X}$ by minimizing Eq. (9)
2. Initialization:
Iteration index: $k = 1$
Error tolerance: ϵ
Maximum iteration number: $K_{\max}$
Regularization parameters: $\lambda_U, \lambda_B, \lambda_1, \lambda_2$
step size: $\delta_\mathbf{U}, \delta_{\mathbf{X}_\mathbf{D}}, \delta_{\mathbf{X}_\mathbf{B}}$
Initial solutions: $\mathbf{U}^{(0)} = \mathbf{X}\mathbf{V}_r$,
3. Reconstruction algorithm for contrast dynamics:
Step 1: Update $\mathbf{U}, \mathbf{X}_\mathbf{D}, \mathbf{X}_\mathbf{B}, \mathbf{\Gamma}_1, \mathbf{\Gamma}_2$ using Eqs. (10–14)
Step 2: Increase iteration index k
Step 3: Stop if $k > K_{\max}$ or $\frac{||\mathbf{X}_\mathbf{D}{}^{(k+1)} - \mathbf{X}_\mathbf{D}{}^{(k)}||_F}{||\mathbf{X}_\mathbf{D}{}^{(k)}||_F} \leq \epsilon$
4. Residual contrast dynamics with background suppression:
Update $\mathbf{X}_\mathbf{B}$ by $\overline{\mathbf{X}}_\mathbf{B} = (\mathbf{I} - \mathbf{U}_\mathbf{M}\mathbf{U}_\mathbf{M}^H)\mathbf{X}_\mathbf{B}$ using Eq. (17)
5. Output: $\mathbf{X}_\mathbf{D}{}^{(k+1)} \rightarrow \mathbf{X}_\mathbf{D}$, $\mathbf{X}_\mathbf{B}{}^{(k+1)} \rightarrow \overline{\mathbf{X}}_\mathbf{B}$, $\mathbf{X}^{(k+1)} \rightarrow \mathbf{X}_\mathbf{D} + \overline{\mathbf{X}}_\mathbf{B}$

The corresponding subspace containing only non-contrast background signals is learned from the following residual signal matrix, $\mathbf{X}_\mathbf{P} = [\mathbf{x}_1 - \mathbf{x}_\mathbf{0}\ \mathbf{x}_2 - \mathbf{x}_\mathbf{0}\ \ldots\ \mathbf{x}_{T_p-1} - \mathbf{x}_\mathbf{0}]$, consisting of difference vectors between the reference and the measured T_p dynamic images before the arrival of CA column by column. However, since the residual signal matrix over T_p phases before the first pass of bolus does not fully reflect motion-induced background changes in the entire dynamic phase, it is extended to accommodate time-varying information by emulating translational, rotational, and random motions. To this end, motion-emulated synthetic vectors, which are generated by performing voxel shifting, voxel rotation, and random rearrangement of neighboring voxels within a reasonable range, are subtracted from the reference and then augmented to the measured matrix $\mathbf{X}_\mathbf{P}$ ($\in \mathbb{C}^{N\times N_p}$) in the column direction as shown in (Park et al., 2017). A basis of the background subspace is then found by performing the SVD on the augmented, residual signal matrix by:

$$[\mathbf{X}_\mathbf{P}\ \ \mathbf{X}_\mathbf{E}] \overset{\text{SVD}}{\rightarrow} \mathbf{U}_\mathbf{B}\mathbf{\Sigma}_\mathbf{B}\mathbf{V}_\mathbf{B}^H \tag{16}$$

where $\mathbf{X}_\mathbf{E}$ ($\in \mathbb{C}^{N\times N_e}$) is the residual signal matrix consisting of motion-emulated synthetic vectors; $\mathbf{U}_\mathbf{B}$ ($\in \mathbb{C}^{N\times r}$) is the left singular matrix that contains the spatial basis of background signals; $\Sigma_\mathbf{B}$ ($\in \mathbb{R}^{r\times r}$) is the diagonal, singular value matrix; $\mathbf{V}_\mathbf{B}$ ($\in \mathbb{C}^{(N_p+N_e)\times r}$) is the right singular matrix.

Given the spatial basis of the background subspace, residual contrast dynamics can be separated from non-contrast background signals by projecting the matrix $\mathbf{X}_\mathbf{B}$ onto the subspace spanned by the basic vectors in $\mathbf{U}_\mathbf{B}$ and then subtracting the projected matrix from $\mathbf{X}_\mathbf{B}$ as:

$$\overline{\mathbf{X}}_\mathbf{B} = (\mathbf{I} - \mathbf{U}_\mathbf{B}\mathbf{U}_\mathbf{B}^H)\mathbf{X}_\mathbf{B} \tag{17}$$

where $\overline{\mathbf{X}}_\mathbf{B}$ is the matrix that contains background-suppressed, residual contrast dynamics; $\mathbf{U}_\mathbf{B}\mathbf{U}_\mathbf{B}^H$ is the projection matrix for background subspace. Complete contrast dynamics is then constructed by $\mathbf{X}_\mathbf{D} + \overline{\mathbf{X}}_\mathbf{B}$. An overall reconstruction of contrast dynamics is summarized in Algorithm 1. Source codes and data in this work will be available online (http://misl.skku.edu).

3. Experiments and Results

To demonstrate the feasibility of the proposed, model-based high-definition DCE MRI in enhancing estimation accuracy of microvascular functions, simulations and experimental studies were performed in patients with brain cancer as follows: (1) Retrospective validation for high-definition contrast dynamics estimation,

(2) Quantitative comparison between high- and low-definition DCE MRIs with varying spatial and temporal resolutions, and (3) Statistical analysis on the effect of spatial and temporal resolution on estimation of microvascular function parameters from the retrospective studies as well as on comparison between the proposed method and conventional routine DCE MRI from the prospective studies.

3.1. Retrospective Validation for High-Definition Contrast Dynamics Estimation

A time series of 3D whole brain DCE data was acquired in 5 patients diagnosed with brain cancer on a 3T whole-body MR scanner (Skyra, Siemens Healthineers, Erlangen, Germany) using a spoiled GRE MR pulse sequence. To achieve high temporal and spatial resolution (1.5 s, 1.0 mm^3) in DCE MRI, each set of 4D data in $k-t$ space was vastly undersampled, in which phase encodings in $k_y - k_z$ space were performed in a pseudo-radial fashion and then subsequently rotated with a golden angle (111.25°) with varying time phases as shown in (Park et al., 2017). Hence, a large portion of phase encodings in each data was prospectively skipped in a different way with time during data acquisition, leading to a very high reduction factor (R) $\sim$ 50. Phase encodings only in a range of intermediate to high frequencies were then shared over three neighboring time phases to reduce signal leakages. Asymmetric sampling (70%) was applied in the readout direction to decrease T_2^* effects. Imaging parameters were: time-of-repetition (TR)/ time-of-echo (TE) = 3.18/1.1 ms, flip angle = 15°, matrix size = 192 × 192 × 144, readout bandwidth = 650 Hz/Px, number of phases = 170, and total imaging time = 4.5 min. Additionally, variable flip angle imaging (Deoni et al., 2005) was performed using 2°, 8°, and 15° to estimate a reference T_{10} map. All imaging protocols were approved by the Institutional Review Board, and written informed consents were obtained from all patients.

To investigate the effectiveness of the proposed method in DCE MRI with error analysis, a set of DCE images without apparent artifacts, which is available from the proposed reconstruction, is chosen as a reference, and then Fourier transformed to produce a fully sampled data in $k-t$ space. The reference image is utilized to evaluate relative performance of reconstruction strategies, which has been often used in other literatures (Lingala et al., 2011; Zhao et al., 2012; Park et al., 2017). The fully sampled DCE data in $k-t$ space are retrospectively under-sampled using a new sampling mask while retaining the same spatial and temporal resolution as the reference, yielding a new set of DCE data.

A set of DCE images was generated using zero-padded inverse FT (Fig. 2a), image difference between the reference and the zero-filled reconstruction (Fig. 2b), main contrast dynamics ($\mathbf{X_D}$) (Fig. 2c), residual CA signals with background artifacts ($\mathbf{X_B}$) (Fig. 2d), background-suppressed residual contrast dynamics ($\overline{\mathbf{X}}_\mathbf{B}$) (Fig. 2e), combined contrast dynamics ($\mathbf{X_D} + \overline{\mathbf{X}}_\mathbf{B}$) (Fig. 2f), a final reconstructed DCE image ($\mathbf{X}_0 + \mathbf{X_D} + \overline{\mathbf{X}}_\mathbf{B}$) (Fig. 2g), and (image difference between the reference and the final reconstructed image (Fig. 2h). The normalized, root-mean-square-error (nRMSE) is calculated by:

$$\text{nRMSE} = \frac{1}{\max(\mathbf{X}_{\text{Ref}})}\sqrt{\frac{1}{\text{N}}\sum_{i=1}^{\text{N}}\left(\text{X}_{\text{Ref},i} - \text{X}_{\text{Rec},i}\right)^2} \tag{18}$$

where i is the pixel index, $\mathbf{X}_{\text{Ref},i}$ is the reference image, and $\mathbf{X}_{\text{Rec},i}$ is the reconstructed image. Incoherent aliasing artifacts in Fig. 2a and b are substantially reduced in Fig. 2g and h. The nRMSE with zero-filled reconstruction is 68% higher than that with the proposed method. Most of CA signals appear in Fig. 2c while a low level of CA and background signals is observed in Fig. 2d. It is noted that background signals in Fig. 2d are further suppressed in Fig. 2e (dotted arrow) while residual contrast dynamics in Fig. 2d is kept in Fig. 2e (solid arrow). Signal time courses in an arterial region (Fig. 3a) and a tissue of interest (Fig. 3b) were correspondingly plotted. $\mathbf{X_D} + \overline{\mathbf{X}}_\mathbf{B}$ describes arterial peak signals more clearly than $\mathbf{X_D}$ (Fig. 3a), while $\mathbf{X_D} + \overline{\mathbf{X}}_\mathbf{B}$ and $\mathbf{X_D}$ appear nearly identical in estimating relatively slowly varying contrast dynamics in a tissue of interest (Fig. 3b).

The effect of the low rank model on signal time courses in arterial and tissue regions was investigated with r = 3, 8, 15, and 30 (Fig. 4). In the AIF (Fig. 4a), signal time courses are: largely underestimated with r = 3, well described with r = 8 and 15, and substantially noisy with r = 30. Likewise, in the output function (Fig. 4b), signal time courses remain nearly identical with r = 8, 15, and 30 while being largely deviant with r = 3. r = 8 was chosen in this work.

The effect of the regularization parameters in Eq. (8) on image reconstruction was investigated by calculating nRMSEs with varying λ_U and λ_B ranging between 1 and 12. Reconstruction errors were the lowest with $\lambda_U = 5$ and $\lambda_B = 7$ while gradually increasing as λ_U and λ_B deviate from the optimal value (Fig. 5a). λ_U and λ_B were set to 5 and 7, respectively. The other parameters were empirically set as follows: $\lambda_1 = 1$, $\lambda_2 = 2$, $\delta_\mathbf{U} = 1.0e^{-7}$, $\delta_{\mathbf{X_D}} = 1.0e^{-6}$, and $\delta_{\mathbf{X_B}} = 1.0e^{-7}$. Additionally, nRMSEs were calculated with several sets of $\delta_\mathbf{U}$, $\delta_{\mathbf{X_D}}$, and $\delta_{\mathbf{X_B}}$ with increasing iterations to demonstrate convergence behavior of the proposed method. nRMSE was converged after roughly 20 $\sim$ 30 iterations with the above chosen values of $\delta_\mathbf{U}$, $\delta_{\mathbf{X_D}}$, and $\delta_{\mathbf{X_B}}$ (Fig. 5b). A typical image reconstruction time was roughly 12 h for each set of data (Xeon CPU 3.2 GHz, 32 GB memory).

To demonstrate the effectiveness of the proposed method in estimating the contrast dynamics, a set of DCE images were reconstructed from the retrospectively undersampled data using the proposed method. To compare with the proposed method, $k-t$ RPCA (Otazo et al., 2015), and $k-t$ SPARSE-SENSE (Feng et al., 2013) were implemented off-line using the MATLAB programming environment with publicly available software. Compared with $k-t$ RPCA and $k-t$ SPARSE-SENSE, the proposed method yields better suppression of background noise and artifacts with superior depiction of structures (enlarged figures in the yellow dotted boxes) and the lowest nRMSE among all comparison methods without apparent noise and artifacts in Fig. 6a and b. Corresponding concentration time courses of CA in an arterial region and a tissue of interest were shown in Fig. 6c and d, respectively. Arterial peak signals are underestimated in $k-t$ RPCA and $k-t$ SPARSE-SENSE while the proposed methods capture the signal evolution more better compared with the reference (Fig. 6c). Moreover, a saturation level of concentration time courses in a tissue of interest is underestimated in $k-t$ RPCA and $k-t$ SPARSE-SENSE while the proposed method is estimated relatively accurate as compared to the reference (Fig. 6d).

Quantitative maps of perfusion and microvascular permeability (F_p, PS, v_p, v_e), which result from the proposed method, $k-t$ RPCA, and $k-t$ SPARSE-SENSE, were then generated (Fig. 7). To this end, signal time course estimates in both arterial regions (input) and brain tissues (output), which reflect contrast dynamics, were converted to concentration time courses in corresponding regions by exploiting the linear relation between concentration of CA and change of T_1 relaxation rate with the pre-defined T_{10} (O'Connor et al., 2011). The AIF was manually measured in a region of the internal carotid artery. Given both the AIF and output functions, perfusion and permeability maps were estimated using nonlinear least squares fitting with the 2CXM mode (Ahearn et al., 2005; Kargar et al., 2018). Compared with $k-t$ RPCA and $k-t$ SPARSE-SENSE, the proposed method estimates apparent bet-

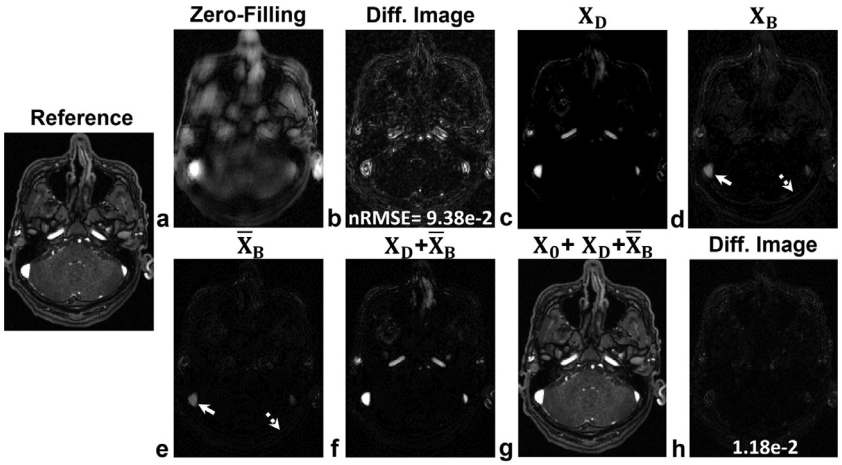

Fig. 2. DCE images reconstructed using: zero-filled inverse Fourier transformation (a), the difference image between the reference and the zero-filled image (b), the proposed method with main CA signals (c), residual CA signals (solid arrow) and backgrounds (dotted arrow) (d), residual CA signals with background suppression (e), combined CA signals (f), a final reconstructed DCE image (g), and the difference image between the reference and the final reconstructied image (h). Note that arterial CA signals in (f) are better estimated with higher signal intensity than those in (c). Additionally, background signals in (d) are well suppressed in (e).

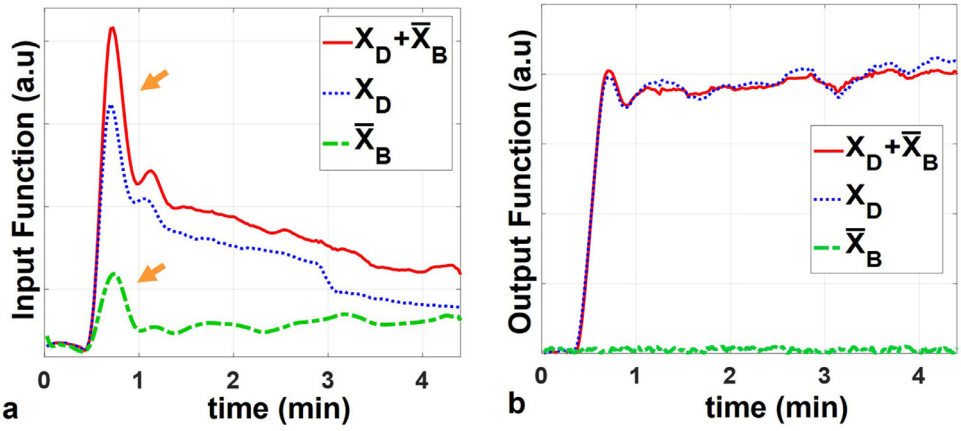

Fig. 3. Signal time courses in DCE MRI for arterial input function (a) and output function (b). Note that $\mathbf{X_D}+\bar{\mathbf{X}}_\mathbf{B}$ estimates a rapidly varying arterial concentrations better than $\mathbf{X_D}$ alone (brown solid arrow) while both $\mathbf{X_D}+\bar{\mathbf{X}}_\mathbf{B}$ and $\mathbf{X_D}$ are nearly identical in describing slowly varying output function.

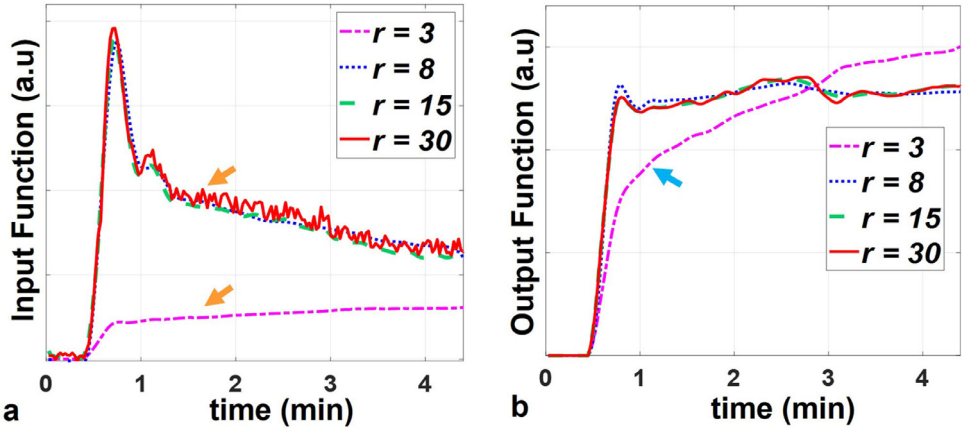

Fig. 4. The effect of the low rank model on signal time courses in an arterial region (a) and a tissue of interest (b) with varying r. Note that signal time courses with $r = 3$ are largely deviant from those with $r = 8$, 15, 30. Additionally, an arterial signal time course appears relatively noisy with $r = 30$.

ter perfusion and permeability values in brain cancer tissues (yellow dotted boxes) in part due to relative accurate depiction of both the input and output functions as compared to reference in Fig. 6c and d. And the nRMSE with the proposed method remains the lowest level compared with $k-t$ RPCA and $k-t$ SPARSE-SENSE.

3.2. Quantitative Comparison between High- and Low-Definition DCE MRI

Since the high-definition reference data (temporal resolution: 1.5 s, spatial resolution: 1.0 mm^3) is available, multiple sets of low-

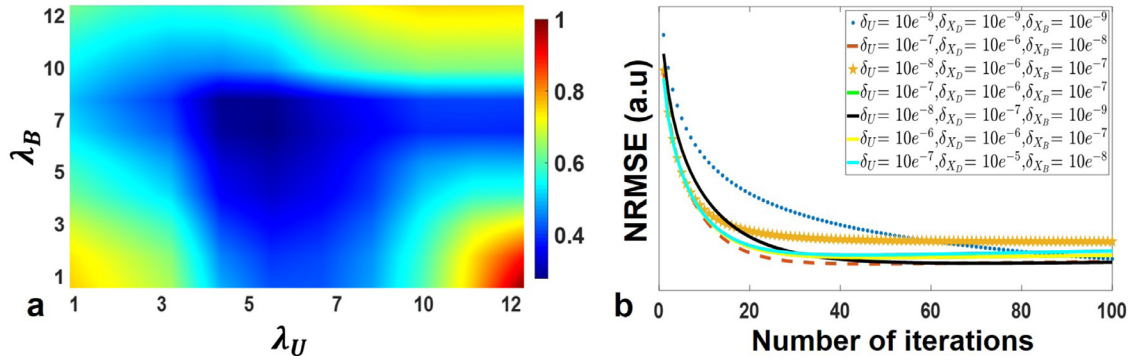

Fig. 5. The parameter sensitivity of the proposed method to λ_U and λ_B with increasing λ_U = [1,12] and λ_B = [1,12], respectively (a) and the convergence behaviors (b). It is noted that the nRMSE of the optimal parameters λ_U =5 and λ_B =7 leads to the lowest nRMSE. And the nRMSE was converged after roughly 20 ~ 30 iterations with the parameters $\delta_{\mathbf{U}} = 1.0e^{-7}$, $\delta_{\mathbf{X_D}} = 1.0e^{-6}$, and $\delta_{\mathbf{X_B}} = 1.0e^{-7}$.

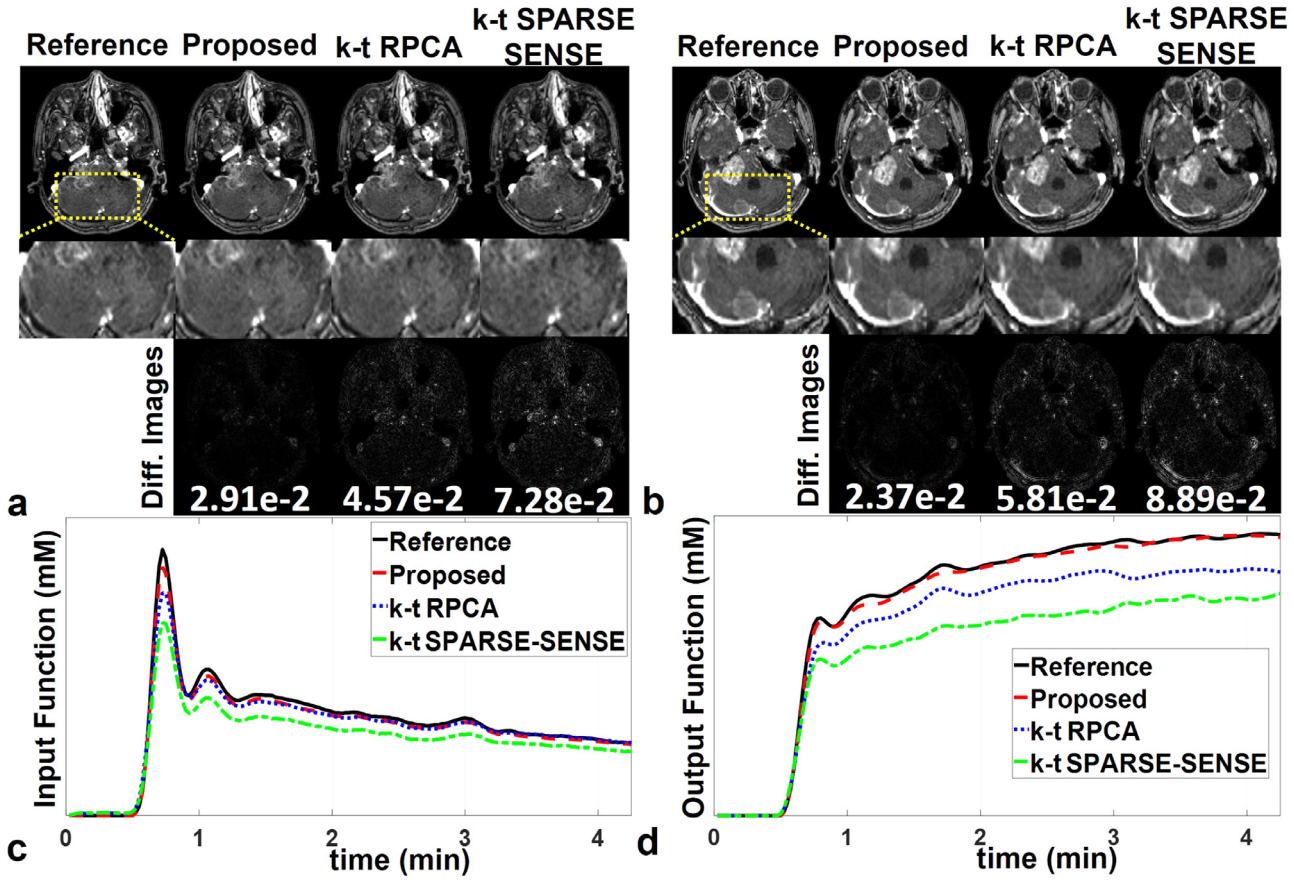

Fig. 6. Comparison of DCE images (a, b) and concentration time courses (c: AIF, d: tissue output function) reconstructed using the proposed method, $k-t$ RPCA, and $k-t$ SPARSE-SENSE. Note that the proposed method (Input region: nRMSE= $2.91e^{-2}$, Output region= $2.37e^{-2}$) yields better suppression of incoherent aliasing artifacts and noise than $k-t$ RPCA (Input region: nRMSE= $4.57e^{-2}$, Output region= $5.81e^{-2}$) and $k-t$ SPARSE-SENSE (Input region: nRMSE= $7.28e^{-2}$, Output region= $8.89e^{-2}$). Furthermore, the proposed method substantially estimates better than the comparison mehods in both input and output functions as compared to the reference.

definition data were emulated with varying resolution to investigate the corresponding effect on the accuracy in estimating contrast dynamics and microvascular function maps.

To investigate the effect of temporal resolution on estimation of contrast dynamics and corresponding perfusion and permeability maps, a time series of the high-definition DCE data was shared over neighboring phases to emulate varying temporal resolutions with 1.5, 4.5, 7.5, and 10.5 s while holding spatial resolution at 1.0 mm^3. Fig. 8 represents concentration time courses in two regions of interest: an arterial region (red dotted circle) (Fig. 8a) and a cancerous tissue (blue dotted circle) (Fig. 8b). With decreasing temporal resolution, an early portion of the AIF is gradually broadened while its peak signal intensity is lowered. Accordingly, an initial upslope of the output function in the cancerous tissue is reduced. It is noted that in overall an initial portion of both the AIF and output functions is heavily affected with varying temporal resolution. Fig. 9 shows perfusion and permeability maps with varying temporal resolution. As temporal resolution is decreased, F_p and PS are gradually underestimated, while v_p and v_e remain identical. It is noted that F_p and PS are microvascular function parameters sensitive to temporal resolution in DCE MRI.

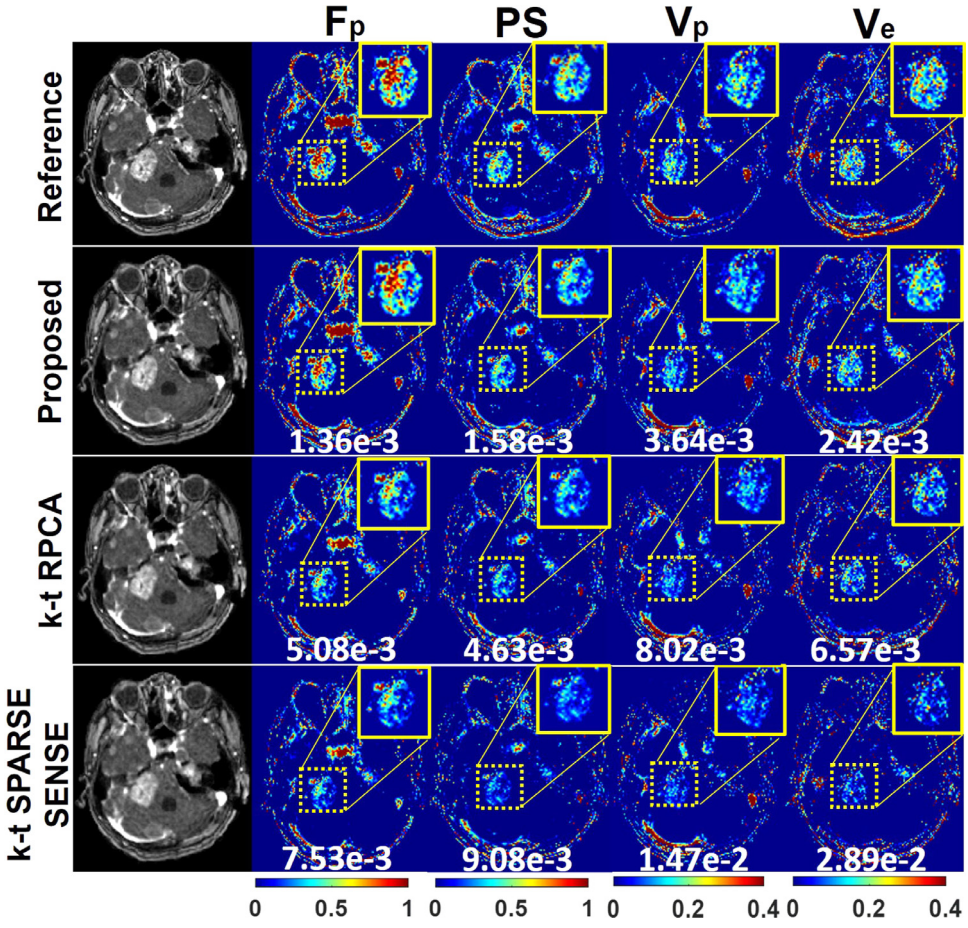

Fig. 7. Quantitative comparison of perfusion (F_p, v_p) and permeability (PS, v_e) maps with the proposed method, $k-t$ RPCA, and $k-t$ SPARSE-SENSE. Note that the proposed method yields higher perfusion and permeability values in brain cancer tissues particularly with F_p and PS than $k-t$ RPCA and $k-t$ SPARSE-SENSE in part due to the highly defined input and output functions as shown in Fig. 6c and d. And the proposed method remain the lowest nRMSE among the comparison methods in all perfusion and permeability maps as compared to the reference.

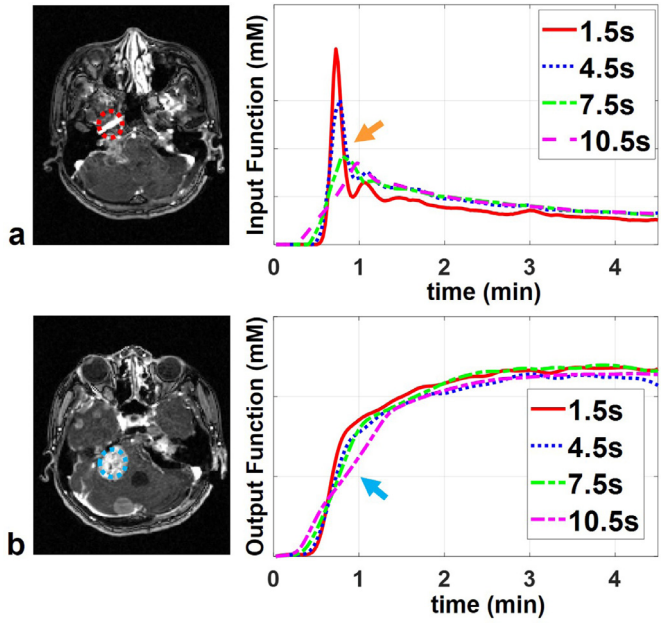

Fig. 8. AIF (a) and tissue output functions (b) reconstructed using the proposed method with varying temporal resolution (1.5, 4.5, 7.5, and 10.5 s). Note that an upslope portion of the input and output functions is gradually underestimated with decreasing temporal resolution (solid arrows).

The effect of spatial resolution on estimation of contrast dynamics and corresponding perfusion and permeability maps was analyzed by emulating DCE data with varying in-plane spatial resolution (1×1 mm^2, 2×2 mm^2, 3×3 mm^2, and 4×4 mm^3) while maintaining temporal resolution at 1.5 s. A through-plane resolution was set to 1.0 mm. To this end, zero-filling was performed on the high-definition reference data for the peripheral region of $k_y - k_z$ space depending on the emulated spatial resolution, and the zero-filled data were then low-pass filtered and inverse Fourier transformed. Fig. 10 represents concentration time courses in an arterial region (red dotted circle) (Fig. 10a) and a cancerous tissue (blue dotted circle) (Fig. 10b). With decreasing spatial resolution, in the AIF an early portion of the concentration time course that includes a peak region is gradually underestimated but its later portion remains similar. On the other hand, in the output function for the cancerous tissue, an initial upslope remains nearly identical despite varying spatial resolution while its later portion gradually saturates to a lower level. It is noted that with varying spatial resolution an initial portion of the AIF and a later portion of the output function are heavily affected. Fig. 11 shows perfusion and permeability maps with varying spatial resolution. Although spatial resolution is decreased, F_p, PS, and v_p seem to remain similar except that v_e are gradually underestimated. It is because the corresponding tissues contain necrosis (low concentration), edema (low concentration), and highly perfused region (high concentration) with a certain level of heterogeneities. Thus, a saturation level of concentration is heavily affected with lowering spatial resolution

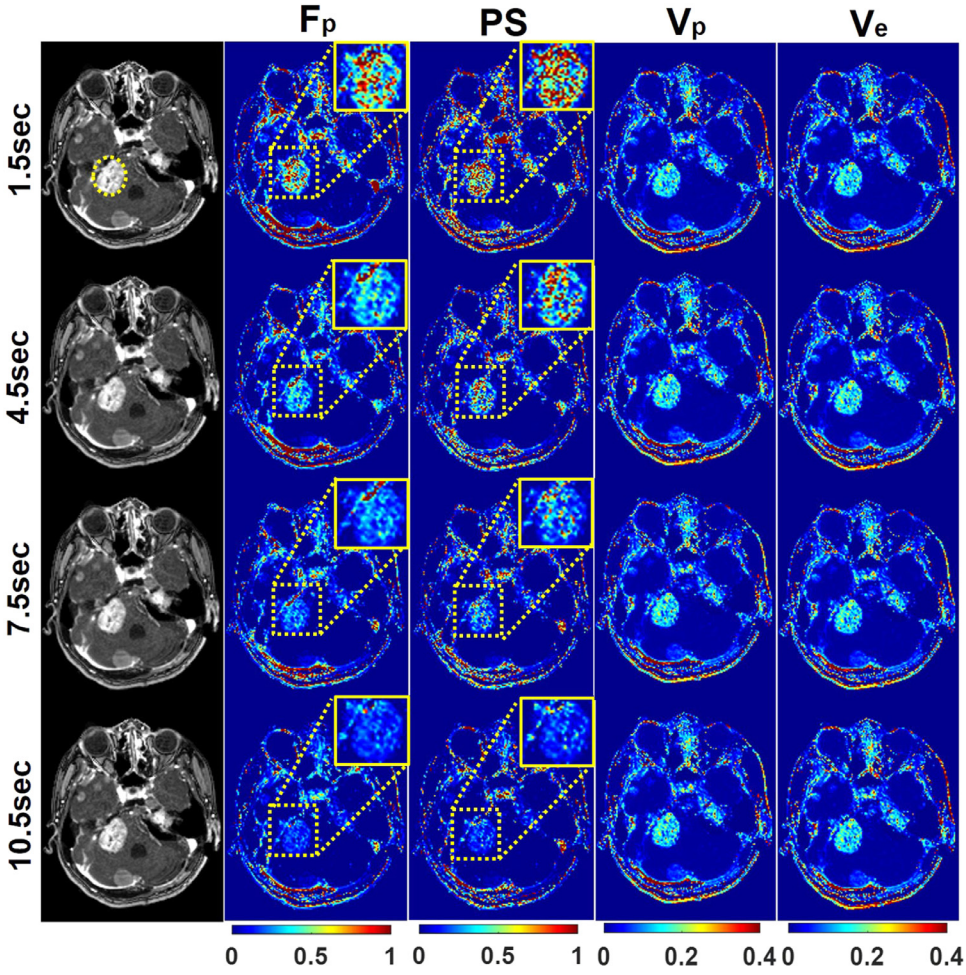

Fig. 9. Comparison of perfusion and permeability maps in the proposed method with varying temporal resolution. Note that with decreasing temporal resolution, F_p and PS are gradually underestimated while v_p and v_e remain nearly identical, suggesting that F_p and PS are the microvascular function parameters sensitive to temporal resolution.

Table 2
Scan parameters for the conventional and experimental high-definition whole-brain DCE MRI.

	Conventional	Proposed
TR	2.85/1.1	3.18/1.1
Flip angle (deg)	15	15
Matrix size	144 × 144 × 40	192 × 192 × 144
FOV	20 × 20 × 12	20 × 20 × 19
Temporal resolutions (s)	4.8	1.5
Spatial resolutions (mm^3)	1.3 × 1.3 × 3 mm^3	1.0 × 1.0 × 1.0 mm^3
Time frames	60	170
Total Scan time (min)	4.8	4.5

due to partial volume effects, which lead to substantial underestimation of the interstitial volume.

Two separate sets of DCE data were prospectively acquired in 30 patients with brain cancer using the proposed, high-definition DCE MRI (1.5 s, 1.0 mm^3) and conventional routine DCE MRI (4.8 s, 1.3 × 1.3 × 3.0 mm^3) for comparison. Imaging protocols are summarized in Table 2. The first set of data was acquired using conventional routine DCE MRI, while roughly two weeks later the second set of data was acquired using the proposed method before surgical operations. In conventional routine DCE MRI, a time series of DCE data was obtained using the TWIST sampling scheme (Laub and Kroeker, 2006) in which k-space was divided into low and high spatial frequency regions and signals in the two regions were then acquired in an alternating fashion. To speed up conventional data acquisition, signals in k-space were undersampled in the phase encoding direction and then shared among three neighboring phases. DCE images were then reconstructed by generalized auto-calibration (Griswold et al., 2002). Fig. 12 compares the proposed method with conventional routine using a pair of DCE brain images (Fig. 12a), concentration time courses in an arterial region (Fig. 12b) and a cancerous tissue (Fig. 12c), and perfusion and permeability maps (Fig. 12d). Compared with conventional routine DCE MRI, the proposed method yields sharper delineation of brain structures as well as highly defined AIF and output functions. Accordingly, quantitative maps in the proposed method exhibit higher values in overall than those in conventional routine DCE MRI, implicating that cancerous tissues are highly perfused and permeable.

3.3. Statistical Evaluation

A two-step statistical analysis was performed on DCE data acquired in 30 patients with brain cancer. The first step is to statistically evaluate the effect of resolution on quantitative maps from the retrospective studies, while the second one is to statistically compare the proposed method with conventional routine DCE MRI from the prospective studies. For all statistical comparisons, SPSS 12 software (SPAA, Inc., Chicago, IL) was employed.

To evaluate the effect of temporal resolution on quantification of microvascular functions, F_p, PS, v_p, and v_e in cancerous tissues from all patients were calculated with the following four tempo-

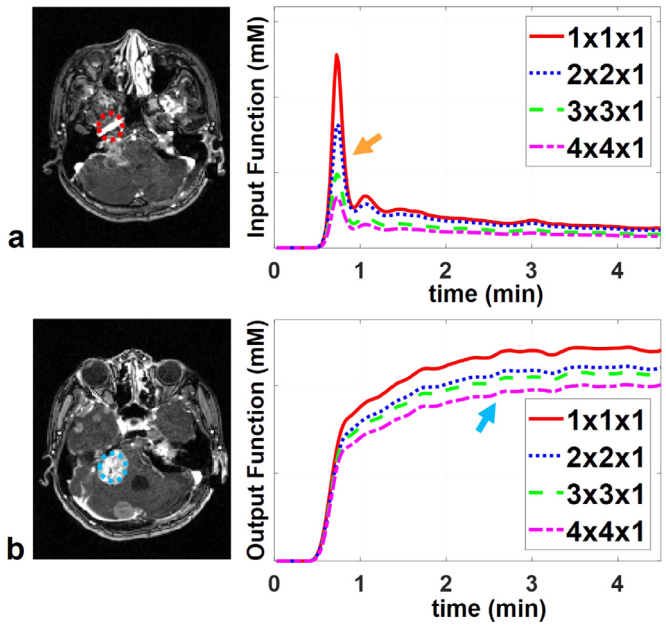

Fig. 10. AIF (a) and tissue output functions (b) reconstructed using the proposed method with varying spatial resolution ($1 \times 1 \times 1$ mm^3, $2 \times 2 \times 1$ mm^3, $3 \times 3 \times 1$ mm^3, $4 \times 4 \times 1$ mm^3). Note that with decreasing spatial resolution, an arterial peak in the input function and a saturation level of concentration time courses in the output function are gradually underestimated (solid arrows).

ral resolutions: 1.5, 4.5, 7.5, and 10.5 s as shown in Figs. 9 and 13 a. Mean microvascular function parameters among the above four temporal resolutions were compared using the repeated measures analysis of variance (ANOVA) with a p-value of 0.05. A p-value for the sphericity assumption was found. With violation of the sphericity assumption, the Greenhouse-Geisser correction was applied. As post hoc analysis, pairwise comparison of mean microvascular functions between two temporal resolutions was performed with the repeated measures ANOVA with Bonferroni adjustment. To evaluate the effect of spatial resolution on quantification of microvascular functions, F_p, PS, v_p, and v_e in cancerous tissues from all patients were calculated with the following four spatial resolutions: $1 \times 1 \times 1$ mm^3, $2 \times 2 \times 1$ mm^3, $3 \times 3 \times 1$ mm^3, $4 \times 4 \times 1$ mm^3 as shown in Figs. 11 and 13 b. Mean microvascular function parameters among the above four spatial resolutions were statistically compared the repeated measures ANOVA with a p-value of 0.05, and pairwise comparison between two spatial resolutions were performed using corresponding post hoc analysis with Bonferroni adjustment. Lastly, mean microvascular function parameters between the proposed high-definition DCE MRI and conventional routine DCE MRI were statistically compared using the repeated measures ANOVA with Bonferroni correction using a p-value of 0.05.

In all statistical analysis, the sphericity assumption is violated ($p \ll 0.05$). The repeated measures ANOVA with the Greenhouse-Geisser correction is then performed. First, the effect of temporal resolution on F_p and PS is statistically significant ($p \ll 0.05$), while the effect of temporal resolution on v_p and v_e is not significant

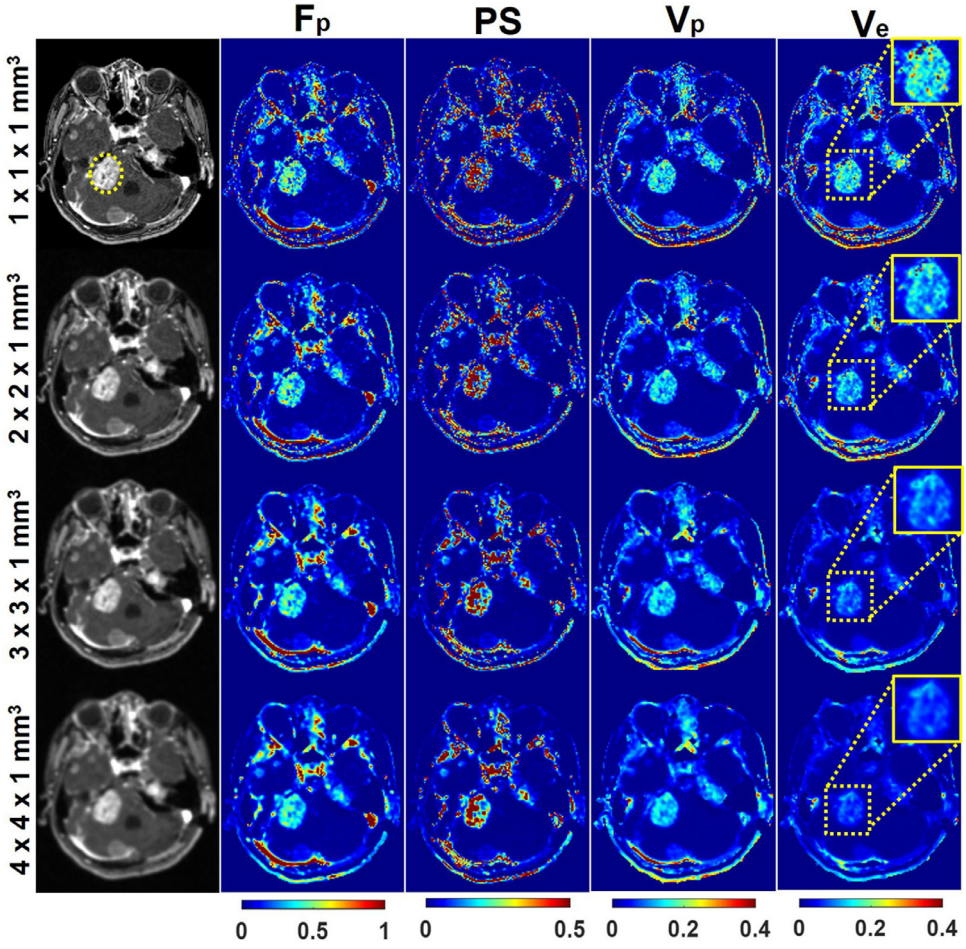

Fig. 11. Comparison of perfusion and permeability maps in the proposed method with varying spatial resolution. Note that with decreasing spatial resolution only v_e is gradually underestimated, suggesting that v_e is the microvascular function parameter sensitive to spatial resolution.

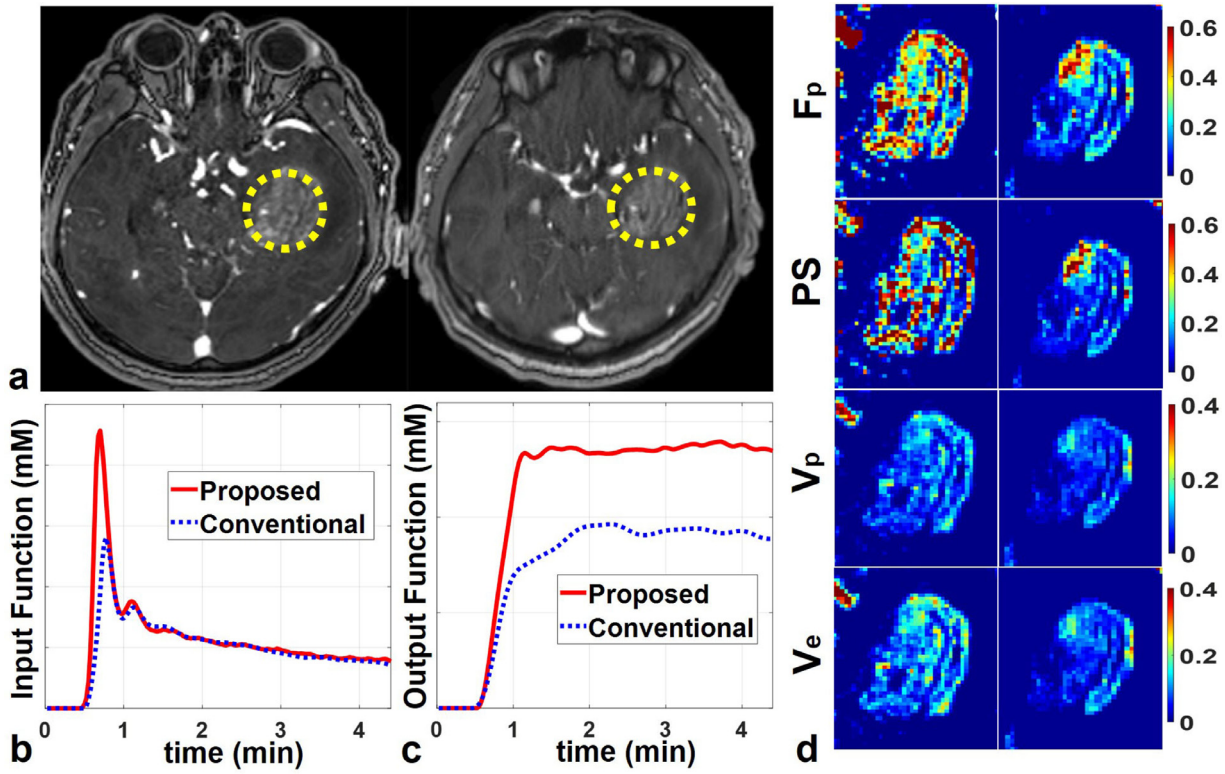

Fig. 12. Comparison of DCE images (a), input (b)) and output (c)) functions, perfusion and permeability maps (d) between the proposed high-definition DCE MRI and conventional routine DCE MRI. Note that compared with conventional DCE MRI the proposed method yields sharper DCE images (a), highly defined input and output functions (b, c), and improved microvascular function parameters (d).

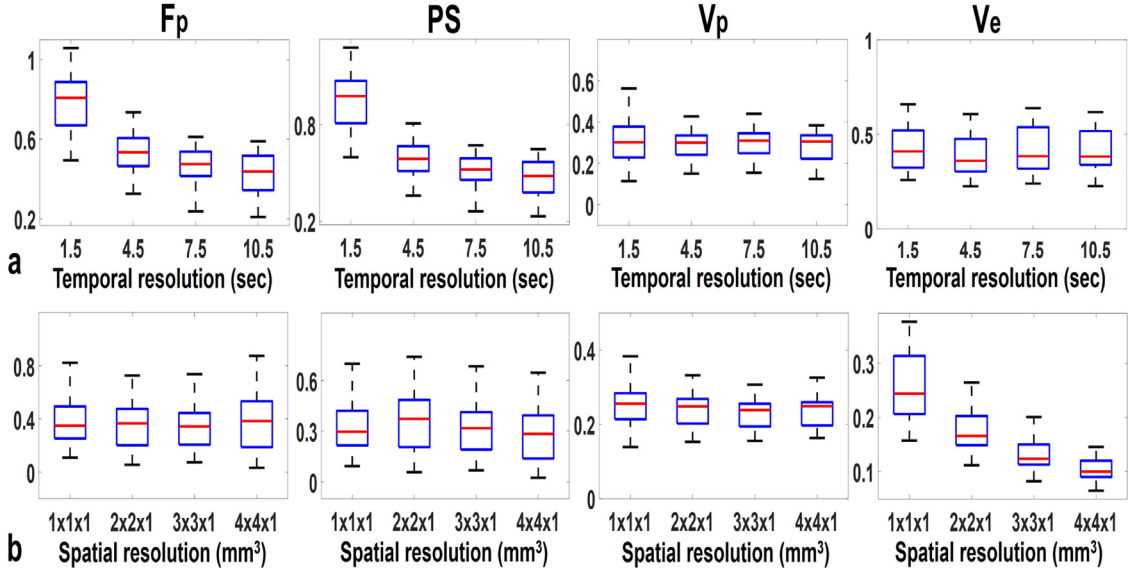

Fig. 13. Mean and deviations of microvascular function parameters for statistical analysis with varying temporal (a) and spatial (b) resolutions. Boxes denote the 25–75 percentiles; horizontal bars indicate the mean; whiskers represent the data range.

with $p = .88$ and $p = .76$, respectively. Post hoc comparison shows that mean F_p difference between 1.5 s and the others is statistically significant ($p \ll 0.05$), but mean F_p differences in the following pairs, 4.5–7.5 s, 4.5–10.5 s, and 7.5–10.5 s, are not significant with $p = .43$, $p = .36$, and $p = 1.00$, respectively. Mean *PS* difference between 1.5 s and the others is statistically significant ($p \ll 0.05$), but mean *PS* differences in the following pairs, 4.5–7.5 s, 4.5–10.5 s, and 7.5–10.5 s, are not significant with $p = .95$, $p = .26$, and $p = .86$, respectively. Second, the effect of spatial resolution on F_p, *PS*, and v_p is not statistically significant with $p = .06$, $p = .14$, and $p = .07$, respectively, while the effect of spatial resolution on v_e is statistically significant ($p \ll 0.05$). Post hoc comparison shows that mean v_e difference between $1 \times 1 \times 1$ mm^3 and the others is statistically significant ($p \ll 0.05$), but mean v_e differences in the following pairs, $2 \times 2 \times 1$ mm^3 – $3 \times 3 \times 1$ mm^3, $2 \times 2 \times 1$ mm^3 – $4 \times 4 \times 1$ mm^3, and $3 \times 3 \times 1$ mm^3 – $4 \times 4 \times 1$ mm^3 are not significant with $p = .26$, $p = 1.00$, and $p = 1.00$. Lastly, mean F_p, *PS*, and v_e differences between the proposed method and con-

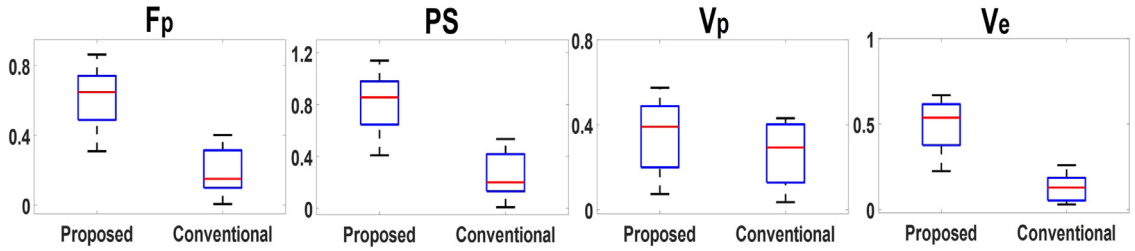

Fig. 14. Mean and deviations of microvascular function parameters for statistical analysis with the proposed and conventional method. Boxes denote the 25–75 percentiles; horizontal bars indicate the mean; whiskers represent the data range.

ventional routine DCE MRI are statistically significant ($p \ll 0.05$), but mean v_p difference between the two methods is not significant with $p = .36$ (Fig. 14).

4. Discussion and Conclusion

Within our knowledge, this is the first work that demonstrates the feasibility of high-definition whole brain DCE MRI in measuring both patient-specific AIF and output functions with high precision (temporal resolution: 1.5 s; spatial resolution: 1.0 mm^3) and hence enabling concurrent estimation of perfusion and microvascular permeability for brain cancer. In this work, it is assumed that a time series of DCE images consists of the following three components in an order of temporal correlations (strong-to-weak): stationary backgrounds, time-varying CA signals, and sporadically occurring irregular signals with time. Signals in the first two components remain identical or smoothly vary with time in a correlated fashion to a certain extent, while those in the third component mainly result from irregular subjection motions and appear temporally uncorrelated. The proposed, model-based high-definition DCE MRI makes the best of the characteristics of the above three components, which are well reflected in the objective function of the proposed constrained reconstruction. That is, in Eq. (8), stationary backgrounds are included in $\mathbf{R_Y}$; temporal correlation of CA signals is implicitly denoted in the low rank matrix factorization, $\mathbf{UV}_r^H$; motion induced incoherent signals appear in $\mathbf{X_B}$ and are then selectively represented in $\mathbf{U_B U_B^H(X_B)}$ of Eq. (17). It is noted that the proposed reconstruction framework, which combines the linearized signal decomposition with the undersampled measurement model in DCE MRI, is inherently well suited to compressed sensing and parallel imaging strategies, enabling highly sparse encodings while traversing a maximum possible distance in $k_y - k_z$ space to achieve high spatial and temporal resolution.

Brain cancer is typically characterized by high vasculature and high permeability due to abnormalities in the endothelial layer (Jain, 1990; Daldrup et al., 1998), resulting in rapid transfer between capillaries and interstitial spaces. Hence, a sampling rate in DCE MRI for brain cancer is, if compared to other applications such as multiple sclerosis, stroke, dementia, etc, to be further pushed to capture contrast dynamics without apparent loss of information particularly in a wash-in portion during the first pass of bolus. Moreover, contrast dynamics in arterial regions is much faster with a larger variance than that in cancerous tissues. To take this issue into account, from the perspective of DCE measurements temporal resolution during data acquisition should be high enough to precisely sample a rapidly varying portion of arterial signal time courses.

To enhance the fidelity of reconstructed CA time courses to DCE measurement data, the rank r in Eq. (7) needs to be increased while the regularization parameters, λ_U and λ_B in Eq. (8) are to be decreased, though noise is amplified. Due to the tradeoff between reconstruction accuracy and noise amplification, r, λ_U, and λ_B are to be properly chosen as shown in Figs. 4 and 5. It is also noted that CA induced signals may not be captured partially in $\mathbf{X_D}$ depending on the values of the above balancing parameters. However, in the proposed mathematical framework of image reconstruction, CA signals are distributed in both $\mathbf{X_D}$ and $\mathbf{X_B}$. In other words, during the alternating minimization process, CA signals, which are potentially missing in $\mathbf{X_D}$, can be subsequently restored in $\mathbf{X_B}$ and then refined in $\overline{\mathbf{X}}_\mathbf{B}$ by exploiting that the basic vectors in $\mathbf{U_B}$, which construct non-contrast features related to signal discrepancies between time phases, do not span a subspace that contain residual CA signals. Thus, the signal leakage problem of CA in the proposed method is alleviated by combining main and residual contrast dynamics components ($\mathbf{X_D} + \overline{\mathbf{X}}_\mathbf{B}$).

Given the above considerations, it is important to precisely define the AIF for quantification of microvascular functions. In conventional DCE MRI, the AIF is found by either measuring an arterial concentration time course directly in patients (patient-specific AIF) or simulating it indirectly with population averaged models (simulated AIF) (Parker et al., 2006). However, it is in practice difficult to measure the AIF because in conventional DCE MRI temporal resolution is readily negotiated with spatial resolution. Although the dual resolution approaches (Jelescu et al., 2011; Li et al., 2012), which utilize low spatial resolution with high temporal resolution for the AIF and high spatial resolution with low temporal resolution for the output function turn out to be effective in capturing contrast dynamics in arterial regions, they are still prone to errors in estimating the AIF due to partial volume effects as shown in Fig. 9. Instead, the AIF can be derived from nonlinear signal models and corresponding fitting procedures using a training group of patients, while being applied to a test group of patients. Nevertheless, since high-definition data in conventional DCE MRI have been in general not available, the simulated approach typically employs low-definition DCE data for the nonlinear fitting process, which may not sufficiently reflect contrast dynamics in arterial regions. Thus, the proposed, model-based high-definition DCE MRI would provide benefits in directly measuring the patient-specific AIF with improved estimation of arterial contrast dynamics as well as in refining the simulated AIF with high sampling.

The proposed method is a two-step approach consisting of interpolation of missing signals in $k - t$ space followed by tracer-kinetic model based estimation of microvascular functions. The previous works in DCE MRI including (Feng et al., 2014; Otazo et al., 2015; Rosenkrantz et al., 2015; Lingala et al., 2017), fall in this category. The proposed method is similar to all previous works in that it employs both inter-channel and spatiotemporal correlations to efficiently reconstruct missing signals from incomplete measurements. The proposed method differs from (Feng et al., 2014; Rosenkrantz et al., 2015) in that the former enforces CA signals in the time dimension to lie in a subspace that can be constructed by only a finite number of basic vectors (low rank model based highly compressible representation) while containing signals with high fidelity to tracer-kinetic models. In (Otazo et al., 2015), DCE images in $x - t$ space are decomposed into stationary component (low rank) and contrast dynamics (sparsity). How-

ever, since CA signals vary in a correlated fashion to a certain extent, contrast dynamics information appears partially in stationary components or is lost. Unlike (Otazo et al., 2015), in the proposed method stationary features are eliminated using the reference as a pre-processing step. Only time-varying information, which includes contrast dynamics and mainly motion-mismatch induced background signals, is then separately modeled and reconstructed. From the perspective of the low rank modeling of contrast dynamics in DCE MRI, the proposed method is similar to (Lingala et al., 2017) though the former deals with CA-driven MR signal time courses while the latter models concentration time courses. However, unlike the proposed method that captures combined contrast dynamics in $\mathbf{X_D} + \overline{\mathbf{X}}_\mathbf{B}$, the low rank approach in (Lingala et al., 2017) may not fully describe rapid patient-specific AIF, potentially yielding erroneous microvascular function maps. On the other hand, one-step approaches (Dikaios et al., 2014; Guo et al., 2017), which incorporate a specific tracer-kinetic model into the measurement model in DCE MRI and produce quantitative microvascular function maps directly from $k - t$ space without image reconstruction, have been recently introduced. However, depending on pathological tissues, a different tracer-kinetic model is to be selected, and the one-step approaches may need to be correspondingly optimized. Additionally, in case a different tracer-kinetic model needs to be applied voxel-wise due to spatial varying tissue environments, the two-step approaches with flexible selection of tissue-adaptive tracer-kinetic models would be preferred.

In conclusion, we successfully demonstrated the feasibility of the proposed, model-based high-definition DCE MRI in brain cancer for concurrent estimation of perfusion and microvascular permeability. It has been difficult to achieve this aim due to limitation of spatial and temporal resolutions in conventional DCE MRI. On the other hand, the proposed method is computationally complex and demanding, requiring 20 to 40 iterations to converge with high accuracy. This computation problem may be alleviated using accelerated parallel computing platforms (multi-CPU and GPU) for smooth translation of the proposed method to a clinical routine. Nevertheless, due to high definition of both the patient-specific input and output functions, the proposed method is expected to widen its clinical utilities to other pathological diseases that accompany blood-brain-barrier leakages, although it remains to be clinically validated in a large group of patients.

Declaration of Competing Interest

The authors declare that they have no known competing financial interests or personal relationships that could have appeared to influence the work reported in this paper.

The authors declare the following financial interests/personal relationships which may be considered as potential competing interests.

Acknowledgment

This work is supported in part by NRF-2016M3C7A1913844, NRF-2017R1A2B4012581, NRF-2018M3C7A1056887, and HI19C0149.

References

Ahearn, T.S., Staff, R.T., Redpath, T.W., Semple, S.I.K., 2005. The use of the Levenberg–Marquardt curve-fitting algorithm in pharmacokinetic modelling of DCE-MRI data. Phys. Med. Biol. 50 (9), N85.

Block, K.T., Uecker, M., Frahm, J., 2007. Undersampled radial MRI with multiple coils. iterative image reconstruction using a total variation constraint. Magn. Reson. Med. 57 (6), 1086–1098.

Boyd, S., Parikh, N., Chu, E., Peleato, B., Eckstein, J., et al., 2011. Distributed optimization and statistical learning via the alternating direction method of multipliers. Found. Trends Signal Process. 3 (1), 1–122.

Brix, G., Kiessling, F., Lucht, R., Darai, S., Wasser, K., Delorme, S., Griebel, J., 2004. Microcirculation and microvasculature in breast tumors: pharmacokinetic analysis of dynamic MR image series. Magn. Reson. Med. 52 (2), 420–429.

Choyke, P.L., Dwyer, A.J., Knopp, M.V., 2003. Functional tumor imaging with dynamic contrast-enhanced magnetic resonance imaging. J. Magn. Reson. Imaging 17 (5), 509–520.

Daldrup, H., Shames, D.M., Wendland, M., Okuhata, Y., Link, T.M., Rosenau, W., Lu, Y., Brasch, R.C., 1998. Correlation of dynamic contrast-enhanced MR imaging with histologic tumor grade: comparison of macromolecular and small-molecular contrast media.. AJR Am. J. Roentgenol. 171 (4), 941–949.

Deoni, S.C., Peters, T.M., Rutt, B.K., 2005. High-resolution T1 and T2 mapping of the brain in a clinically acceptable time with DESPOT1 and DESPOT2. Magn. Reson. Med. 53 (1), 237–241.

Dikaios, N., Arridge, S., Hamy, V., Punwani, S., Atkinson, D., 2014. Direct parametric reconstruction from undersampled (k, t)-space data in dynamic contrast enhanced MRI. Med. Image Anal. 18 (7), 989–1001.

Dutoit, J.C., Vanderkerken, M.A., Verstraete, K.L., 2013. Value of whole body MRI and dynamic contrast enhanced MRI in the diagnosis, follow-up and evaluation of disease activity and extent in multiple myeloma. Eur. Radiol. 82 (9), 1444–1452.

Feng, L., Grimm, R., Block, K.T., Chandarana, H., Kim, S., Xu, J., Axel, L., Sodickson, D.K., Otazo, R., 2014. Golden-angle radial sparse parallel MRI: combination of compressed sensing, parallel imaging, and golden-angle radial sampling for fast and flexible dynamic volumetric MRI. Magn. Reson. Med. 72 (3), 707–717.

Feng, L., Srichai, M.B., Lim, R.P., Harrison, A., King, W., Adluru, G., Dibella, E.V., Sodickson, D.K., Otazo, R., Kim, D., 2013. Highly accelerated real-time cardiac cine MRI using $k - t$ SPARSE-SENSE. Magn. Reson. Med. 70 (1), 64–74.

Garpebring, A., Ostlund, N., Karlsson, M., 2009. A novel estimation method for physiological parameters in dynamic contrast-enhanced MRI: application of a distributed parameter model using Fourier-domain calculations. IEEE Trans. Med. Imaging 28 (9), 1375–1383.

Goldstein, T., Osher, S., 2009. The split Bregman method for L1-regularized problems. SIIMS 2 (2), 323–343.

Griswold, M.A., Jakob, P.M., Heidemann, R.M., Nittka, M., Jellus, V., Wang, J., Kiefer, B., Haase, A., 2002. Generalized autocalibrating partially parallel acquisitions (grappa). Magn. Reson. Med. 47 (6), 1202–1210.

Guo, Y., Lebel, R.M., Zhu, Y., Lingala, S.G., Shiroishi, M.S., Law, M., Nayak, K., 2016. High-resolution whole-brain DCE-MRI using constrained reconstruction: prospective clinical evaluation in brain tumor patients. Med. Phys. 43 (5), 2013–2023.

Guo, Y., Lingala, S.G., Zhu, Y., Lebel, R.M., Nayak, K.S., 2017. Direct estimation of tracer-kinetic parameter maps from highly undersampled brain dynamic contrast enhanced MRI. Magn. Reson. Med. 78 (4), 1566–1578.

Hackstein, N., Kooijman, H., Tomaselli, S., Rau, W.S., 2005. Glomerular filtration rate measured using the patlak plot technique and contrast-enhanced dynamic MRI with different amounts of gadolinium-DTPA. J. Magn. Reson. Imaging 22 (3), 406–414.

Ingrisch, M., Sourbron, S., Morhard, D., Ertl-Wagner, B., Kümpfel, T., Hohlfeld, R., Reiser, M., Glaser, C., 2012. Quantification of perfusion and permeability in multiple sclerosis: dynamic contrast-enhanced MRI in 3D at 3T. Invest Radiol. 47 (4), 252–258.

Jain, R.K., 1990. Vascular and interstitial barriers to delivery of therapeutic agents in tumors. Cancer Metast Rev. 9 (3), 253–266.

Jansen, S.A., Fan, X., Karczmar, G.S., Abe, H., Schmidt, R.A., Newstead, G.M., 2008. Differentiation between benign and malignant breast lesions detected by bilateral dynamic contrast-enhanced MRI: a sensitivity and specificity study. Magn. Reson. Med. 59 (4), 747–754.

Jelescu, I., Leppert, I., Narayanan, S., Araújo, D., Arnold, D., Pike, G., 2011. Dual-temporal resolution dynamic contrast-enhanced MRI protocol for blood–brain barrier permeability measurement in enhancing multiple sclerosis lesions. J. Magn. Reson. Imaging 33 (6), 1291–1300.

Kargar, S., Borisch, E.A., Froemming, A.T., Kawashima, A., Mynderse, L.A., Stinson, E.G., Trzasko, J.D., Riederer, S.J., 2018. Robust and efficient pharmacokinetic parameter non-linear least squares estimation for dynamic contrast enhanced MRI of the prostate. Magn. Reson. Imaging 48, 50–61.

Kershaw, L.E., Cheng, H.-L.M., 2010. Temporal resolution and SNR requirements for accurate DCE-MRI data analysis using the AATH model. Magn. Reson. Med. 64 (6), 1772–1780.

Khalifa, F., Soliman, A., El-Baz, A., El-Ghar, M.A., El-Diasty, T., Gimel'farb, G., Ouseph, R., Dwyer, A.C., 2014. Models and methods for analyzing DCE-MRI: a review. Med. Phys. 41 (12).

Laub, G., Kroeker, R., 2006. Syngo twist for dynamic time-resolved MR angiography. Magn. Flash 3, 92–95.

Lebel, R.M., Jones, J., Ferre, J.-C., Law, M., Nayak, K.S., 2014. Highly accelerated dynamic contrast enhanced imaging. Magn. Reson. Med. 71 (2), 635–644.

Li, K.-L., Buonaccorsi, G., Thompson, G., Cain, J.R., Watkins, A., Russell, D., Qureshi, S., Evans, D.G., Lloyd, S.K., Zhu, X., et al., 2012. An improved coverage and spatial resolution—using dual injection dynamic contrast-enhanced (ICE-DICE) MRI: a novel dynamic contrast-enhanced technique for cerebral tumors. Magn. Reson. Med. 68 (2), 452–462.

Lingala, S.G., Guo, Y., Lebel, R.M., Zhu, Y., Bliesener, Y., Law, M., Nayak, K.S., 2017. Tracer kinetic models as temporal constraints during DCE-MRI reconstruction. Magn. Reson. Med.

Lingala, S.G., Hu, Y., DiBella, E., Jacob, M., 2011. Accelerated dynamic MRI exploiting sparsity and low-rank structure: $k - t$ SLR. IEEE Trans. Med. Imaging 30 (5), 1042–1054.

Merali, Z., Huang, K., Mikulis, D., Silver, F., Kassner, A., 2017. Evolution of blood--brain-barrier permeability after acute ischemic stroke. PLoS ONE 12 (2), e0171558.
O'Connor, J., Tofts, P., Miles, K., Parkes, L., Thompson, G., Jackson, A., 2011. Dynamic contrast-enhanced imaging techniques: CT and MRI. Br. J. Radiol. 84 (special_issue_2), S112–S120.
O'Connor, J.P., Jackson, A., Parker, G.J., Jayson, G.C., 2007. DCE-MRI Biomarkers in the clinical evaluation of antiangiogenic and vascular disrupting agents. Br. J. Cancer 96 (2), 189.
van Osch, M.J., van der Grond, J., Bakker, C.J., 2005. Partial volume effects on arterial input functions: shape and amplitude distortions and their correction. J. Magn. Reson. Imaging 22 (6), 704–709.
Otazo, R., Candès, E., Sodickson, D.K., 2015. Low-rank plus sparse matrix decomposition for accelerated dynamic MRI with separation of background and dynamic components. Magn. Reson. Med. 73 (3), 1125–1136.
Park, S., Kim, E.Y., Sohn, C.-H., Park, J., 2017. Dynamic contrast-enhanced MR angiography exploiting subspace projection for robust angiogram separation. IEEE Trans. Med. Imaging 36 (2), 584–595.
Parker, G.J., Roberts, C., Macdonald, A., Buonaccorsi, G.A., Cheung, S., Buckley, D.L., Jackson, A., Watson, Y., Davies, K., Jayson, G.C., 2006. Experimentally-derived functional form for a population-averaged high-temporal-resolution arterial input function for dynamic contrast-enhanced MRI. Magn. Reson. Med. 56 (5), 993–1000.
Roberts, H.C., Roberts, T.P., Brasch, R.C., Dillon, W.P., 2000. Quantitative measurement of microvascular permeability in human brain tumors achieved using dynamic contrast-enhanced MR imaging: correlation with histologic grade. Am. J. Neuroradiol. 21 (5), 891–899.
Rosenkrantz, A.B., Geppert, C., Grimm, R., Block, T.K., Glielmi, C., Feng, L., Otazo, R., Ream, J.M., Romolo, M.M., Taneja, S.S., et al., 2015. Dynamic contrast-enhanced MRI of the prostate with high spatiotemporal resolution using compressed sensing, parallel imaging, and continuous golden-angle radial sampling: preliminary experience. J. Magn. Reson. Imaging 41 (5), 1365–1373.
Simpson, N.E., He, Z., Evelhoch, J.L., 1999. Deuterium NMR tissue perfusion measurements using the tracer uptake approach: I. Optimization of methods. Magn. Reson. Med. 42 (1), 42–52.
Sourbron, S., Buckley, D.L., 2011. Tracer kinetic modelling in MRI: estimating perfusion and capillary permeability. Phys. Med. Biol. 57 (2), R1.
Sourbron, S., Ingrisch, M., Siefert, A., Reiser, M., Herrmann, K., 2009. Quantification of cerebral blood flow, cerebral blood volume, and blood–brain-barrier leakage with DCE-MRI. Magn. Reson. Med. 62 (1), 205–217.
Sourbron, S.P., Buckley, D.L., 2013. Classic models for dynamic contrast-enhanced MRI. NMR Biomed. 26 (8), 1004–1027.
St.Lawrence, Ting-Yim, L., 1998. An adiabatic approximation to the tissue homogeneity model for water exchange in the brain: I. Theoretical derivation. J. Cerebr. Blood F. Met. 18 (12), 1365–1377.
Tofts, P.S., Kermode, A.G., 1991. Measurement of the blood-brain barrier permeability and leakage space using dynamic MR imaging. 1. fundamental concepts. Magn. Reson. Med. 17 (2), 357–367.
Van De Haar, H.J., Burgmans, S., Jansen, J.F., Van Osch, M.J., Van Buchem, M.A., Muller, M., Hofman, P.A., Verhey, F.R., Backes, W.H., 2016. Blood-brain barrier leakage in patients with early alzheimer disease. Radiology. 281 (2), 527–535.
Wang, Y., Yang, J., Yin, W., Zhang, Y., 2008. A new alternating minimization algorithm for total variation image reconstruction. SIIMS 1 (3), 248–272.
Zhao, B., Haldar, J.P., Christodoulou, A.G., Liang, Z.-P., 2012. Image reconstruction from highly undersampled (k, t)-space data with joint partial separability and sparsity constraints. IEEE Trans. Med. Imaging 31 (9), 1809–1820.